

Unified tensor network theory for frustrated classical spin models in two dimensions

Feng-Feng Song,^{1,*} Tong-Yu Lin,^{1,*} and Guang-Ming Zhang^{1,2,3,†}

¹*State Key Laboratory of Low Dimensional Quantum Physics and
Department of Physics, Tsinghua University, Beijing 100084, China*

²*Collaborative Innovation Center of Quantum Matter, Beijing 100084, China*

³*Frontier Science Center for Quantum Information, Beijing 100084, China*

(Dated: September 12, 2023)

Frustration is a ubiquitous phenomenon in many-body physics that influences the nature of the system in a profound way with exotic emergent behavior. Despite its long research history, the analytical or numerical investigations on frustrated spin models remain a formidable challenge due to their extensive ground state degeneracy. In this work, we propose a unified tensor network theory to numerically solve the frustrated classical spin models on various two-dimensional (2D) lattice geometry with high efficiency. We show that the appropriate encoding of emergent degrees of freedom in each local tensor is of crucial importance in the construction of the infinite tensor network representation of the partition function. The frustrations are thus relieved through the effective interactions between emergent local degrees of freedom. Then the partition function is written as a product of a one-dimensional (1D) transfer operator, whose eigen-equation can be solved by the standard algorithm of matrix product states rigorously, and various phase transitions can be accurately determined from the singularities of the entanglement entropy of the 1D quantum correspondence. We demonstrated the power of our unified theory by numerically solving 2D fully frustrated XY spin models on the kagome, square and triangular lattices, giving rise to a variety of thermal phase transitions from infinite-order Brezinskii-Kosterlitz-Thouless transitions, second-order transitions, to first-order phase transitions. Our approach holds the potential application to other types of frustrated classical systems like Heisenberg spin antiferromagnets.

I. INTRODUCTION

Frustrated spin systems have become an extremely active field of theoretical and experimental research in the last decades characterized by complex low-energy physics and fascinating emergent phenomena¹⁻³. A system is regarded as frustrated when conflicting interaction terms are present, featured by the inability to minimize total energy by concurrently reducing the energy of each group of interacting degrees of freedom. Frustration underlies non-trivial behavior across physical systems or more general many-body systems, as the minimization of local conflicts gives rise to new degrees of freedom^{4,5}.

Classical frustrated spin systems can be understood as simplified quantum mechanical models which employ classical spins to investigate the behavior of strongly correlated magnetic systems with competing interactions. The existence of frustration depends on the lattice geometry and/or the nature of the interactions⁶. For example, the anti-ferromagnetic (AF) Ising model defined by a set of spins of $s = \pm 1$ is frustrated on the triangular and kagome lattices with massive ground-state degeneracy^{7,8}. However, AF Ising models are not frustrated on the 2D square lattice because the lattice is bipartite and the energy can be simply minimized by the Neel configuration of alternating spins. Frustration also depends on the dimension of the spin variables. For the frustrated AF XY spin systems composed of planar vectors $\vec{s} = (\sin \theta, \cos \theta)$, the ground-state configuration is usually highly degenerate with new symmetries induced from non-collinear patterns. The new degrees of freedom can give rise to rich and complex phases at finite temperatures, which have

been studied over the past decades on the square⁹⁻²⁴, the triangular²⁵⁻³³ and the kagome lattices³⁴⁻⁴⁰.

The study of frustrated classical spin systems is important not only for understanding the emergent behavior of physical systems like spin glasses^{41,42} but also for general optimization problems across multiple disciplines⁴³. Considerable efforts have been made in the investigation of the fundamental properties of frustrated classical spin systems. Despite decade-long efforts, a generic approach to dealing with frustrated spin systems with both high accuracy and high efficiency is still lacking. Well-established methods such as Monte Carlo simulations, mean-field theories, and renormalization group techniques, have made significant contributions to the study of the classical frustrated spin models. However, they have encountered many difficulties such as low efficiency or limited applications^{39,44-46}.

Recent progress in the tensor network methods provides new computational approaches for studying classical lattice models with strong frustrations^{24,40,47-49}. It is found that the construction of the tensor network of the partition function is nontrivial for frustrated systems compared to the standard formulation. For example, the ground state local rules should be encoded in the local tensors to satisfy the ground state configurations induced by geometrical frustrations⁴⁷. In the frustrated Ising models, a linear searching algorithm based on a Hamiltonian tessellation has been proposed to find the proper transitional invariant unit^{48,49}. In the frustrated XY models, the idea of splitting of $U(1)$ spins and dual transformations have been developed to overcome the convergence issues^{24,40}. Although these techniques

make a success in specific models, they seem to be very tricky. Thus, one wonders whether there exists a general framework to treat frustrated classical spin models.

Here, we generalize the underlying principles of the tensor network representation to make it applicable to generic frustrated classical spin systems. When comprising the whole tensor network of the partition function, the crucial point is that the emergent degrees of freedom induced by frustrations should be encoded in the local tensors. In this way, the massive degeneracy is characterized by emergent dual variables such as height variables in the AF Ising model on the triangular lattice^{50,51} and chiralities in frustrated XY models^{38,40}. The emergent variables capture the freedom of a group of interacting spins under the constraint of frustrations. In the sense of coarse-graining, the local tensors carry the effective interactions between emergent local degrees of freedom. The local tensors usually sit on the dual sites of the original lattice which can be constructed from dual transformations. It is worth noting that the dual transformations should be imposed on the whole cluster of a number of spins in correspondence with the emergent dual variables.

We demonstrate the power of the generalized theory of tensor network representation by applying it to fully frustrated XY models on the kagome, triangular, and square lattices. First of all, we can express the infinite 2D tensor network as a product of 1D transfer matrix operators, which can be contracted efficiently by recently developed tensor network algorithms under optimal variational principles⁵²⁻⁵⁴. Then, from the singularity of the entanglement entropy of the 1D quantum transfer operator, various phase transitions can be determined with great accuracy according to the same criterion⁵⁵. Finally we find that a broad array of emergent physics has been treated including various types of phase transitions from first-order, second-order to the Berezinskii-Kosterlitz-Thouless (BKT) phase transitions. The complex phase structures of the frustrated XY systems are revisited and clarified with new tensor network solutions. The present approach holds the potential application to next-nearest-neighbor frustrated spin systems and other types of classical spins like Heisenberg antiferromagnet.

The rest of the paper is organized as follows. In Sec. II, we introduce the theory of tensor network representations for classical frustrated spin models with two concrete examples. After constructing the tensor networks of Ising spin antiferromagnets on the kagome and triangular lattices, we perform the numerical calculation of the residual entropy of the frustrated Ising models, which are comparable to the exact results. In Sec. III, we apply the unified theory to the fully frustrated XY spin models on the kagome, square, and triangular lattices, and present the numerical results for the determination of the finite temperature phase diagram of frustrated XY systems, especially the AF triangular XY model and the modified square XY model. Finally in Sec. IV, we discuss the future generalizations of the method and give our conclusions. In the Appendix, we outline the detailed tensor

network methods for numerical calculations.

II. TENSOR NETWORK REPRESENTATIONS OF 2D STATISTICAL MODELS

A. Emergent degrees of freedom

Tensor networks have proven to be a very potent tool in the study of strongly correlated quantum models as well as classical statistical mechanics. To implement this powerful method, the first step is to convert the partition function of a classical lattice model with local interactions into a tensor network representation.

The standard construction of the tensor network is conducted by putting a matrix on each bond of the original lattice accounting for the Boltzmann weight of the nearest-neighboring interactions⁵⁶. For a generic spin model with nearest-neighbor interactions

$$H = \sum_{\langle i,j \rangle} h(s_i, s_j), \quad (1)$$

the partition function can be decomposed into a tensor network as a product of local Boltzmann weights,

$$Z = \sum_{\{s_i\}} e^{-\beta H(\{s_i\})} = \sum_{\{s_i\}} \prod_{\langle i,j \rangle} W(s_i, s_j), \quad (2)$$

where $\langle i, j \rangle$ refers to the nearest neighbors, s_i are the spin variables, and the interaction matrices are given by

$$W(s_i, s_j) = e^{-\beta h(s_i, s_j)}, \quad (3)$$

whose row and column indices are the spin variables shown in Fig. 1. The δ tensors on the lattice vertexes ensure all indices of W take the same value at the joint point.

Furthermore, we perform the Schmidt decomposition on the symmetric matrix W

$$W(s_i, s_j) = (U\sqrt{S})(\sqrt{S}V^\dagger) = V_a(s_i, s_k)V_b(s_k, s_j), \quad (4)$$

and the partition function can be cast into the uniform tensor network representation as shown in Fig. 1

$$Z = \text{tTr} \prod_i O_{s_1, s_2}^{s_3, s_4}(i) \quad (5)$$

by grouping all V matrices that connect to the δ tensors

$$O_{s_1, s_2}^{s_3, s_4} = \sum_{s_k} V_b(s_1, s_k)V_b(s_2, s_k)V_a(s_k, s_3)V_a(s_k, s_4). \quad (6)$$

The standard representation has been successfully applied to many lattice statistical models without frustration⁵⁵⁻⁵⁹. However, it cannot be implemented directly in the frustrated spin models, where the tensor network contraction algorithms fail to converge. It was

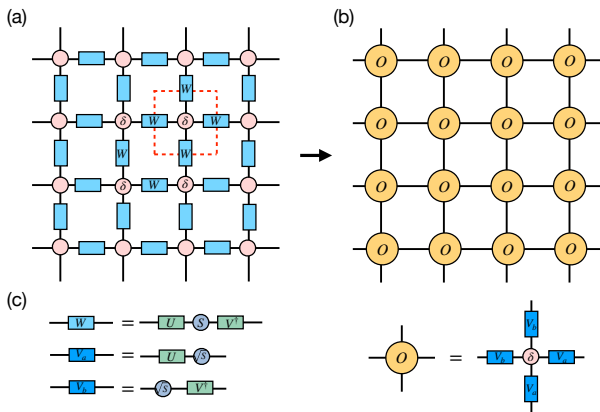


FIG. 1: The standard construction of the tensor network. (a) The W matrix represents the Boltzmann weight on each link, and the δ tensor on each site represents the sharing of the same spin between neighboring W matrices. (b) The tensor network representation of the partition function composed of uniform local tensors. (c) The local tensor O is built by the singular value decomposition (SVD) on each W matrix and the grouping of the V matrices connecting to the δ tensors.

found that the proper encoding of the ground state local rules in local tensors was crucial for the contraction to converge. To fulfill the physics of the ground state manifold, a linear algorithm was proposed to search for the optimal Hamiltonian tessellation for Ising antiferromagnets^{48,49}. The key point is that the energy of all local ground state configurations should be simultaneously minimized under the splitting of the global Hamiltonian into local groups of interactions. And the local tensors are constructed as translational units coinciding with the local clusters of the tessellation.

In order to extend tensor network approaches to generic frustrated classical spin models, we should understand the ground state local rules from a more fundamental perspective of emergent degrees of freedom. In frustrated systems, new degrees of freedom often emerge as a result of the minimization of local conflicts. The ground state of frustrated spin systems is highly degenerate because a number of spins can behave as free spins. Such freedom can therefore be represented by a set of emergent variables describing the effective interactions induced by frustrations. For some models, the emergent variables can be derived directly like height variables in the AF Ising triangular model^{50,51} and chiralities in frustrated XY models^{38,40}. For the spin models with more complicated interactions, the emergent variables may not be explicitly expressed but they can still be characterized by local tensors composed of a cluster of local interactions^{48,49}. This idea generalizes tensor network approaches readily to classical frustrated systems of both discrete and continuous spins.

Before discussing the tensor network construction of the frustrated spin model, we give some examples of emergent degrees of freedom by revisiting the exactly

solvable frustrated models. One of the simplest frustrated spin models is the AF Ising model on the kagome lattice

$$H = J \sum_{\langle i,j \rangle} \sigma_i \sigma_j, \quad (7)$$

where $J > 0$ denotes the AF interactions between nearest-neighbor spins $s_i = \pm 1$ as displayed in Fig. 2 (a).

The kagome AF Ising model is disordered at all temperatures with an extensive ground state degeneracy characterized by a finite residual entropy⁸. To minimize the energy of each triangular plaquette, three spins should obey the ground state local rule of “two up one down, one down two up” as shown in Fig. 2 (a).

Besides directly focusing on the local spin configurations, the physics of the model can be understood from the emergent degrees of freedom on the triangle centers. A set of charge variables can be defined at each triangle

$$Q_u = \sum_{i \in \Delta} s_i, \quad Q_d = - \sum_{i \in \nabla} s_i, \quad (8)$$

where Δ and ∇ denote the upward and downward triangles. The Hamiltonian can then be expressed as

$$H = \frac{J}{2} \sum_{p \in \Delta(\nabla)} (Q_p^2 - 3) \quad (9)$$

in terms of the topological charges Q_p .

Although there seems to be no explicit interaction between charges in the Hamiltonian, the variables Q_p are not independent because the shared spin between the neighboring triangles should be the same. The constraints between neighboring charges can be naturally represented by a link between local tensors as a Kronecker delta tensor in the language of tensor networks. In this way, the interactions between Ising spins are transformed into a charge model including the self-energy of the charges and the effective interactions between these charges. The charge variables can take four values $Q = \pm 1, \pm 3$ at finite temperatures. In the zero temperature limit, the charges of $Q = \pm 3$ are energetically suppressed. The “two up one down, one up two down” rule corresponds to charge variables $Q = \pm 1$ allowed by the ground state manifold.

The emergent charge variables can also be applied to the triangular lattice in the same spirit as the case of the kagome lattice. The triangular AF Ising model in Fig. 3 (a) can be transformed into

$$H = \frac{J}{2} \sum_{\langle i,j \rangle \in p} s_i s_j = \frac{J}{4} \sum_p (Q_p^2 - 3), \quad (10)$$

where the only difference is that each nearest-neighbor triangles share two same spins. The charges variables help us to understand why the tiling of $p \in \Delta(\nabla)$ is crucial for the triangular lattices⁴⁸. The reason is that the tessellation of only one type of triangle fails to characterize the interactions between the emergent charge variables.

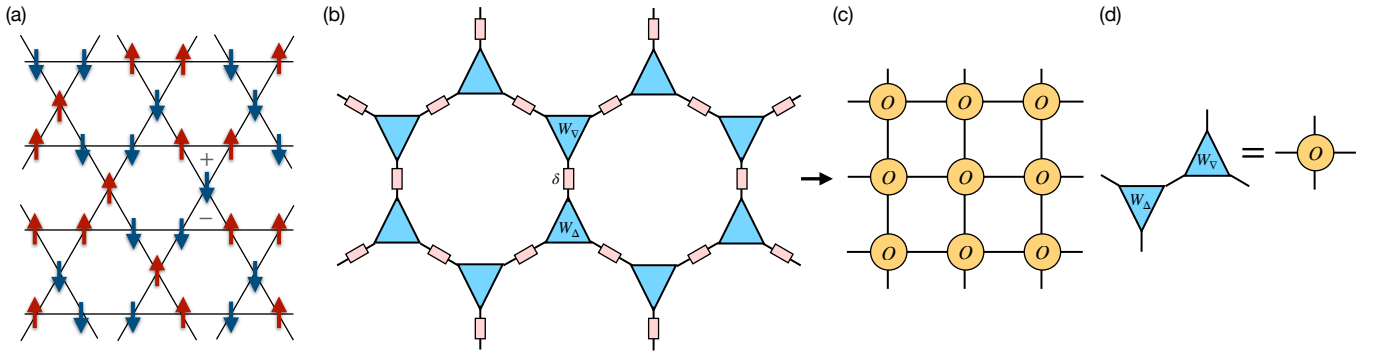


FIG. 2: Tensor network representation of the AF Ising model on a kagome lattice. (a) One of the ground state configurations on the kagome lattice with $Q = \pm 1$ charges on each triangle. (b) Putting the W_Δ (W_∇) tensors on the centers of the upward (downward) triangles to represent the self-energy of the charge variables, where the δ tensors between the nearest neighbor triangles can be translated into the connections of tensor legs directly. (c) The tensor network representation of the partition function composed of uniform local O tensors. (d) The construction of O tensor by contracting neighboring W_Δ and W_∇ tensors.

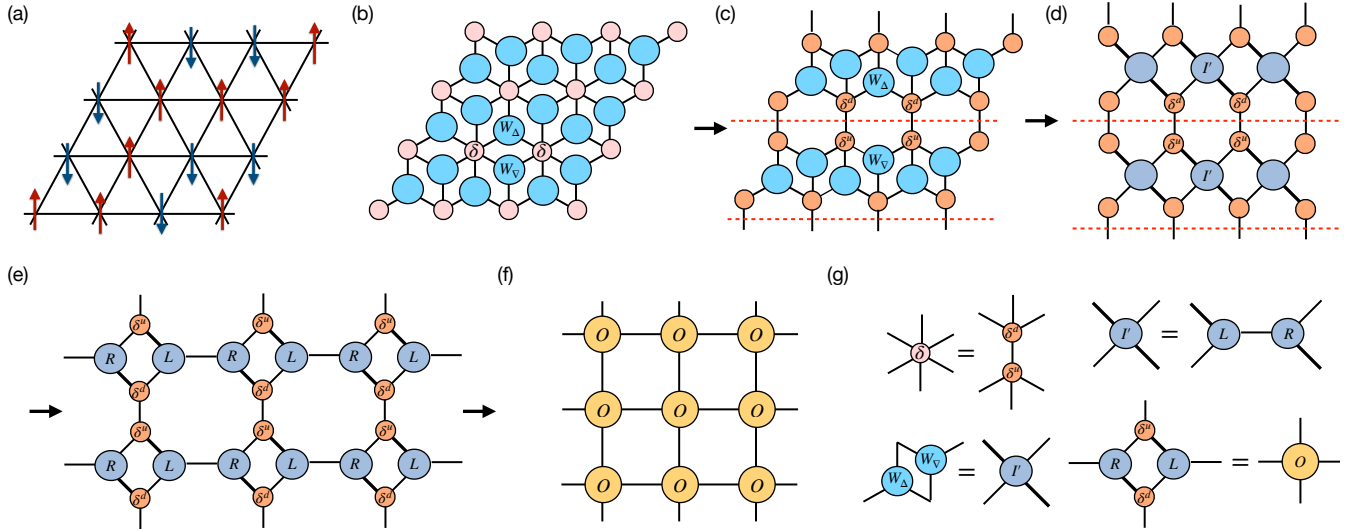


FIG. 3: Tensor network representations of the Ising anti-ferromagnet on a triangular lattice. (a) One of the massive degenerate ground state configurations. (b) The W_∇ and W_Δ tensors are defined on the center of the triangles. The pink δ tensor represents a six-legged Kronecker delta tensor which connects the W_∇ and W_Δ tensors surrounding it. (c)-(d) The construction of row-to-row transfer matrix by splitting the six-legged δ tensors vertically and regrouping the index of a pair of neighboring W_∇ and W_Δ tensor into an I' tensor. (e)-(f) The construction of the local uniform tensor O by splitting I' horizontally and grouping with δ^u and δ^d tensors. (g) The details of the operations on local tensors during the construction procedure.

B. General principle for tensor network construction

Now we can build up a general principle for the tensor network representation of frustrated spin models. The key point is that the emergent degrees of freedom should be encoded in each local tensor in the construction of the infinite tensor network for the partition function. Since the emergent degrees of freedom is universal in frustrated systems, the generic approach can be applied to classical frustrated systems of both discrete and continuous symmetries. Moreover, the finite-temperature properties can

also be probed when the interactions among emergent degrees of freedom are faithfully captured.

In practice, it is not necessary to write down the explicit model of the interactions between emergent variables. The effective interactions are implicit in the connections between local tensors. Each local tensor constituting the Boltzmann weight should carry the emergent degrees of freedom corresponding to a unit cluster of spins. From this perspective, the breakdown of standard construction in the triangular Ising model⁴⁸ can be understood: the emergent degrees of freedom located on the downward triangles are lost in the infinite tensor net-

work contraction.

We summarize the general procedure to construct the tensor network representation of the frustrated spin models as follows:

- i). Identify the emergent degree of freedom, usually located on the dual site, and the corresponding geometry cluster composed of classical spins.
- ii). Reformulate the partition function into the form of

$$Z = \sum_{\{s\}} \prod_c W_c(c) \prod_{\langle c, c' \rangle} W_l(c, c') \delta_{c, c'} \quad (11)$$

where c enumerates all the clusters, W_c and W_l correspond to the Boltzmann weight of all the spin configurations $\{s\}$ within a cluster and between neighboring clusters, and δ tensors ensure the shared spins between different clusters be the same. For continuous spins, the W tensors should be transformed onto a discrete basis via the Fourier transformation.

- iii). Split and regroup the W tensors to build regular local tensors constituting an infinite uniform tensor network representation of the partition function.

C. Kagome and triangular AF Ising models as two examples

The general principle can be applied directly to classical frustrated models with discrete symmetries. The tensor network representation of the kagome AF Ising model (7) can be built simply based on the emergent charge variables defined in (8). As displayed in Fig. 2 (b), we first split the global Boltzmann weight into local Boltzmann weights on each triangle. Then the partition function of the AF Ising model can be written as

$$Z = \sum_{\{s_i\}} \prod_p W_p(s_1, s_2, s_3), \quad (12)$$

where the Boltzmann weight on each upward and downward triangle is expressed by a three-legged W tensor

$$W_p(s_1, s_2, s_3) = e^{-\beta J(s_1 s_2 + s_2 s_3 + s_3 s_1)}. \quad (13)$$

The constraint of sharing the same spin between a pair of neighboring W tensors is imposed by the Kronecker delta tensor.

Then the transitional invariant local tensor O is achieved by combining a pair of upward and downward triangles

$$O_{s_1, s_2}^{s_3, s_4} = \sum_{s_5} W_{\Delta}(s_1, s_2, s_5) W_{\nabla}(s_5, s_3, s_4) \quad (14)$$

as displayed in Fig. 2 (d), and the uniform tensor network representation of the partition function in Fig. 2 (c) is given by

$$Z = \text{tTr} \prod_i O_{s_1, s_2}^{s_3, s_4}(i) \quad (15)$$

where “tTr” means the tensor contraction over all auxiliary links and i denotes the sites of the transitional invariant unit.

The above tensor network can be contracted efficiently using standard algorithms for infinite systems with extremely high accuracy^{52,53,55}. In the zero temperature limit, the tensor W can be reduced to the same tensor obtained in the Ref.⁴⁸, yielding a residual entropy of $S_0 \approx 0.501833$, consistent with the exact result⁸.

For the triangular AF Ising model displayed in Fig. 3 (a), the tensor network representation can be constructed in a similar way. The only difference is that each spin is shared by six surrounding triangles. As shown in Fig. 3 (b), the constraint between the triangular plaquettes is realized through the six-legged delta tensors

$$\delta_{s_1, s_2, s_3, s_4, s_5, s_6} = \begin{cases} 1, & s_1 = s_2 = s_3 = s_4 = s_5 = s_6 \\ 0, & \text{otherwise} \end{cases} \quad (16)$$

and the tensor W is defined in the same way as the kagome AF Ising model Eq. (13).

To construct a row-to-row transfer matrix, we split the six-legged delta tensors vertically as two four-legged delta tensors

$$\delta_{s_1, s_2, s_3, s_4, s_5, s_6} = \sum_{s_7 = \pm 1} \delta_{s_1, s_2, s_3, s_7}^u \delta_{s_7, s_4, s_5, s_6}^d \quad (17)$$

as shown in Fig. 3 (c). Then a pair of W_{Δ} and W_{∇} are grouped into a tensor I' as shown in Fig. 3 (d). The tensor I' can be further split horizontally as displayed in Fig. 3 (e)

$$I' = LR \quad (18)$$

by a singular-value decomposition

$$I' = USV^\dagger, \quad (19)$$

where U and V^\dagger are three-legged unitary tensors, S is a semi-positive diagonal matrix and

$$L = U\sqrt{S}, \quad R = \sqrt{S}V^\dagger. \quad (20)$$

Finally, the regular local tensor O is obtained by grouping δ^u , δ^d , and a pair of L and R tensors. The details are depicted in Fig. 3 (g). This gives a uniform tensor-network representation of the partition function

$$Z = \text{tTr} \prod_i O_{s_1, s_2}^{s_3, s_4}(i) \quad (21)$$

as displayed in Fig. 3 (f). Although the local tensor O is slightly different from the one constructed by the method of Hamiltonian tessellation⁴⁸, the tensor network is well defined and can be readily generalized to frustrated systems with continuous symmetries discussed in the following parts.

As shown in Fig. 4 (a), standard contraction algorithms^{52,53,60} display a nice convergence at both zero

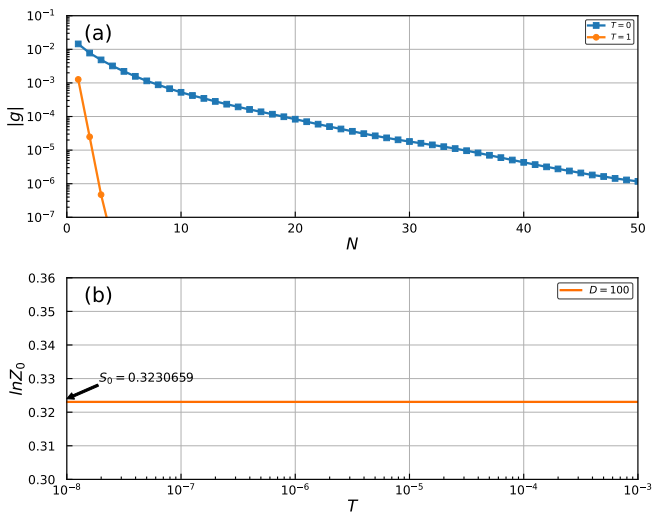


FIG. 4: Numerical results of the Ising anti-ferromagnet on the triangular lattice, the bond dimension of uniform MPS is $D = 100$. (a) Convergence of the VUMPS algorithm at $T = 1$ and $T = 0$. $|g|$ is the convergence measure in the VUMPS algorithm and N is the number of iteration steps. (b) $\ln Z_0$ as a function of temperature. The residual entropy per site is $S_0(D = 100) = 0.3230659$, which is the same as the exact result to seven decimal places.

temperature and finite temperatures. The numerical calculation of the expectation value of the magnetization

$$m = \langle s_i \rangle = \frac{1}{N} \sum_i s_i \quad (22)$$

is found to be zero under all temperatures, indicating the absence of the long-range order (LRO). Moreover, the ground state residual entropy is calculated as displayed in Fig. 4 (b)

$$S_0 = \frac{1}{N} \ln Z_0 \approx 0.323065, \quad (23)$$

in good agreement with the exact result⁷.

III. TENSOR NETWORK THEORY FOR 2D FULLY FRUSTRATED XY SPIN MODELS

A. Duality transformation and split of $U(1)$ spins

In this section, we demonstrate the power of the generic idea of emergent degrees of freedom by the implementations in the frustrated model with a continuous $U(1)$ symmetry. The frustrated XY models, to some extent, are “less frustrated” than the Ising ones. The XY spins have more freedom to rotate on the plane to minimize local conflict interactions, but the Ising spins are constrained to only two orientations. That is why there exists quasi-LRO in the frustrated XY spin models at low temperatures, while the frustrated Ising models are

usually disordered even at zero temperature. Despite a long history of investigations^{9–40}, many properties of the frustrated XY spin systems are still not well understood.

In both frustrated and non-frustrated XY models, a widely accepted and established analytical tool is the 2D Coulomb gas representation^{61–63}. However, the form of Coulomb gas formulation is obtained through an approximate approach^{61,62} and it is hard to directly represent the charge variables by original phase variables^{22,64}. Instead, we can comprehend the topological charge, located on the dual sites, as a coarse-grained degree of freedom formed by a cluster of phase variables located on the original plaquette. This understanding serves as a fundamental perspective for constructing the tensor network of the frustrated XY spin models.

Our tensor network approach provides a universal tool to deal with frustrated systems on various lattice geometries. We can reformulate the partition function into a general form of in the same way as the Ising case

$$Z = \prod_i \int \frac{d\theta_i}{2\pi} \prod_p W_p(\{\theta_p\}) \quad (24)$$

where p denotes the plaquette of the lattice and W_p corresponds to the Boltzmann weight of the elementary cluster. However, different from the Ising case studied in the Ref.⁴⁸, one may encounter two technical issues when constructing a tensor network based on (24). First, the indices of local tensors are continuous spin variables, which is hard to treat in the framework of tensor networks. So the Fourier transformation is necessary to bring the local tensors onto a discrete basis. Second, the Kronecker delta functions describing the constraints of the sharing spins are changed to the Dirac delta functions. For the Ising spin cases, the shared spins are split and connected directly by the Kronecker delta functions. Such a strategy cannot be simply extended for the case of continuous spins because the loops of the Dirac delta functions are not well defined. This problem can be overcome by introducing an auxiliary spin connecting to the shared spins between different clusters.

B. AF XY spin model on a kagome lattice

To describe the Josephson junction array under a uniform external magnetic field^{9,37}, the frustrated XY model on a kagome lattice in Fig. 5 (a) is defined by the Hamiltonian

$$H = -J \sum_{\langle i,j \rangle} \cos(\theta_i - \theta_j - A_{ij}) \quad (25)$$

where $J > 0$ is the coupling strength, i and j are the lattice sites, and the summation is over all pairs of the nearest neighbors. The frustration in this model is induced by the gauge field defined on the lattice bond satisfying $A_{ij} = -A_{ji}$. The case of full frustration corresponds to

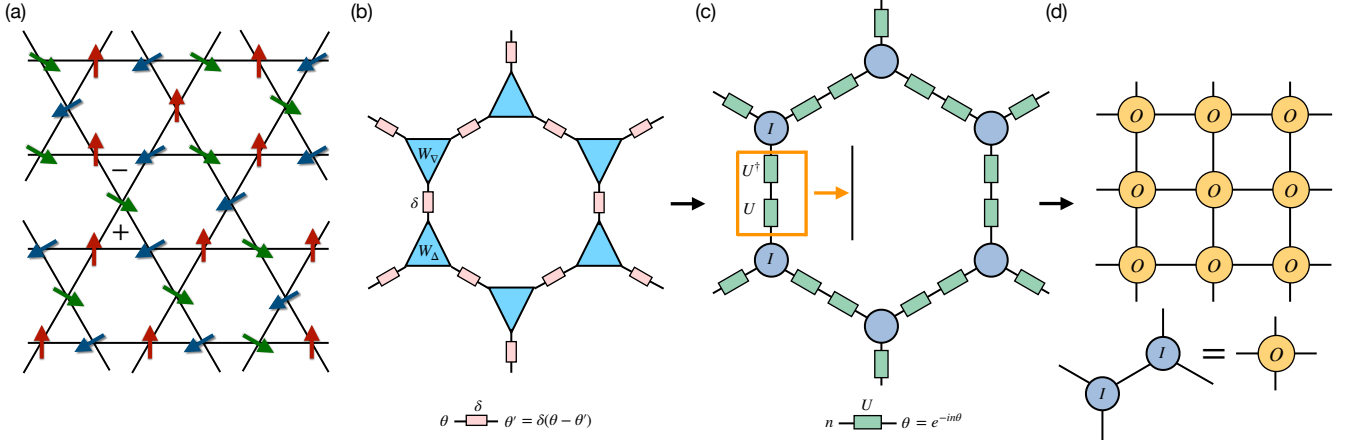


FIG. 5: Tensor network representation of the fully frustrated XY model on the kagome lattice. (a) One of the ground state configurations. The positive and minus signs denote the chiralities on the triangular plaquettes. (b) The tensor network with continuous indices. The W_Δ and W_∇ tensors represent the Boltzmann weight on up and down-type triangles. The δ matrix represents the Dirac delta function. (c) The construction of tensor network with discrete indices by making Fourier transformation on each triangle plaquette and integrating out $\{\theta\}$ variables. (d) The tensor network representations composed of local uniform tensor O , where the O tensor is built by combining two neighboring I tensors

one-half flux quantum per plaquette,

$$f = \frac{1}{2\pi} \sum_{\langle i,j \rangle \in \Delta} A_{ij} = \frac{1}{2}, \quad (26)$$

where the sum is taken around the perimeter of a plaquette. We can choose the fixed gauge condition of $A_{ij} = \pm\pi$ on each bond of the triangular plaquettes, and the model is transformed into an AF XY model on the kagome lattice

$$H = J \sum_{i,j} \cos(\theta_i - \theta_j). \quad (27)$$

The ground state of this model can be obtained by simultaneously minimizing the energy on each elementary triangle. As shown in Fig. 5(a), the phase difference between each pair of neighboring spins should be $\pm 2\pi/3$, which gives rise to the emergent degrees of freedom of chiralities $\tau = \pm 1$, corresponding to the anti-clockwise and clockwise rotation of the spins around the plaquette. The ground state of the AF XY model on a kagome lattice has a massive accidental degeneracy described by the fluctuations of the chiralities.

To capture the emergent degrees of freedom induced by frustrations in the construction of the tensor network, we divide the Hamiltonian into local terms on each triangle:

$$H = \sum_p H_p, \quad (28)$$

where H_p includes all the interactions within an elementary triangle

$$H_p = J \sum_{\langle i,j \rangle \in p} \cos(\theta_i - \theta_j). \quad (29)$$

The partition function can now be written as

$$Z = \prod_i \int \frac{d\theta_i}{2\pi} \prod_p W_p, \quad (30)$$

where $W_p = e^{-\beta H_p}$ is a three-legged tensor with continuous $U(1)$ indices and the constraint of sharing the same spin at the corners is realized by the Dirac delta function $\delta(\theta_i - \theta'_i)$, as shown in Fig. 5 (b).

To transform the local tensors onto a discrete basis, we employ the duality transformation to the whole upward triangles

$$I_{n_1, n_2, n_3} = \prod_{i=1}^3 \int \frac{d\theta_i}{2\pi} W_\Delta(\theta_1, \theta_2, \theta_3) U_{n_1}(\theta_1) U_{n_2}(\theta_2) U_{n_3}(\theta_3),$$

and the downward triangles

$$I'_{n_1, n_2, n_3} = \prod_{i=1}^3 \int \frac{d\theta_i}{2\pi} W_\nabla(\theta_1, \theta_2, \theta_3) U_{n_1}^\dagger(\theta_1) U_{n_2}^\dagger(\theta_2) U_{n_3}^\dagger(\theta_3),$$

where

$$U_n(\theta) = e^{-in\theta} \quad (31)$$

are the basis of the Fourier transformation. Since W_p is unchanged under the spin reflection of $\theta \rightarrow -\theta$, we have $I_{n_1, n_2, n_3} = I'_{n_1, n_2, n_3}$ as displayed in Fig. 5 (c). Meanwhile, the duality transformation on the Dirac delta function gives the Kronecker delta function

$$\int \frac{d\theta}{2\pi} U_{n_1}^\dagger(\theta) U_{n_2}(\theta) = \delta_{n_1, n_2}. \quad (32)$$

Finally, the translation-invariant local tensor O is achieved by combining a pair of I tensors and we arrive at the uniform tensor network representation of

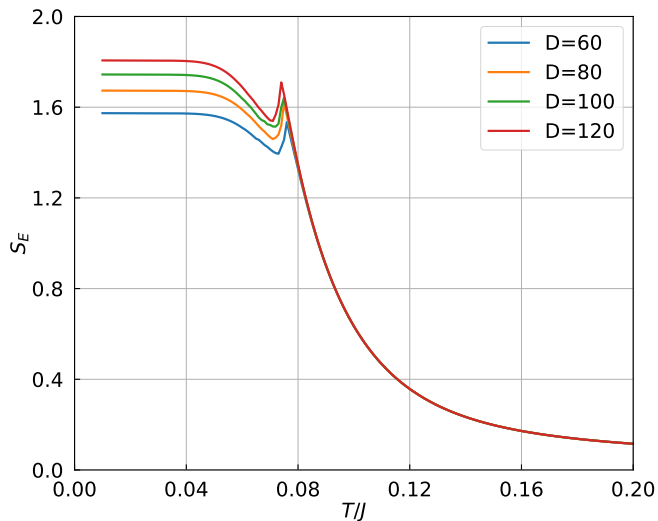


FIG. 6: The entanglement entropy as a function of temperature under different MPS bond dimensions for the AF XY spin model on the kagome lattice.

the partition function

$$Z = \text{tTr} \prod_i O_{s_1, s_2}^{s_3, s_4}(i) \quad (33)$$

as shown in Fig. 5 (d). In fact, the same tensor network has been also obtained in a less straightforward way with the help of the infinite summation, where the interactions between emergent variables can be seen clearly⁴⁰. A direct comparison to the problematic standard construction in Ref.⁴⁰ demonstrates the importance of encoding the emergent degree of freedom in the local tensors: besides the proper Hamiltonian tessellation, the duality transformation is also necessary to capture the essential physics of the chiralities.

In the framework of tensor networks, the entanglement entropy of the fixed-point MPS for the 1D quantum correspondence exhibits singularity at the critical temperatures, offering a sharp criterion to determine possible phase transitions in the thermodynamic limit. As shown in Fig. 6, by employing the tensor network method outlined in the Appendix, the entanglement entropy S_E develops only one sharp singularity at the critical temperature $T_c \simeq 0.075J$, indicating that a single BKT phase transition takes place at a rather low temperature. The peak positions are almost unchanged with different MPS bond dimensions ranging from $D = 60$ to 120 . Thus, the transition temperature is determined with high precision, which is in good agreement with theoretical predictions for the unbinding temperature of $1/3$ vortex pairs^{36,38,40}. The low-temperature phase of the model can be interpreted as the presence of charge-6e superconductivity (SC) in the absence of charge-2e SC⁴⁰.

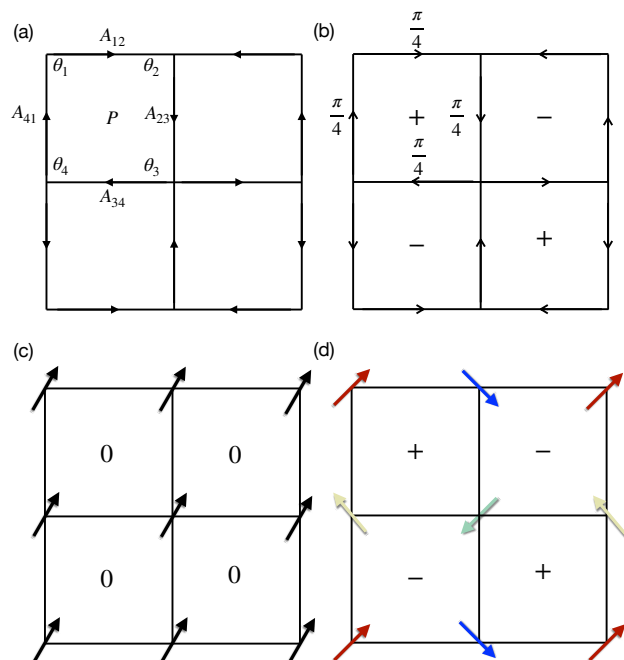


FIG. 7: (a) The fully frustrated XY model on a square lattice. The arrows on the links correspond to the gauge field A_{ij} with the value of $\pm \pi/4$. The sign of A_{ij} is denoted by the direction of the arrow. (b) The ground state of the FFXY model on a square lattice with a checkerboard pattern of chirality. (c) The ground state of the modified XY model for $\frac{\mu}{J} < \frac{1}{8}$. (d) The ground state of the modified XY model for $\frac{\mu}{J} > \frac{1}{8}$. The $0, \pm$ signs correspond to the topological charges located on the centers of the plaquettes.

C. Fully Frustrated XY spin model on a square lattice

The fully frustrated XY (FFXY) spin model on a 2D square lattice can be defined with gauge fields on the lattice bonds

$$H = -J \sum_{\langle i,j \rangle} \cos(\theta_i - \theta_j - A_{ij}), \quad (34)$$

where the full frustration corresponds to the uniform gauge field of $A_{ij} = \pi/4$ on each bond of the square plaquettes. As displayed in Fig. 7 (b), the minimum of the Hamiltonian is obtained when all gauge-invariant phase differences between nearest-neighbor spins $\phi_{i,j} = \theta_i - \theta_j - A_{ij}$ equal to $\pm \pi/4$. The ground state can be characterized by a checkerboard pattern of chiralities $\tau = \pm 1$ defined by $\sum_{\square} \phi_{i,j} = \tau\pi$. Another degenerate state can be obtained by switching the positive and negative chiralities. Therefore, in addition to the $U(1)$ symmetry, the chiralities give rise to an emergent Z_2 degeneracy of the ground state of the FFXY model on a square lattice^{24,41,65}.

To obtain the tensor network representation of the partition function, we first divide the global Hamiltonian

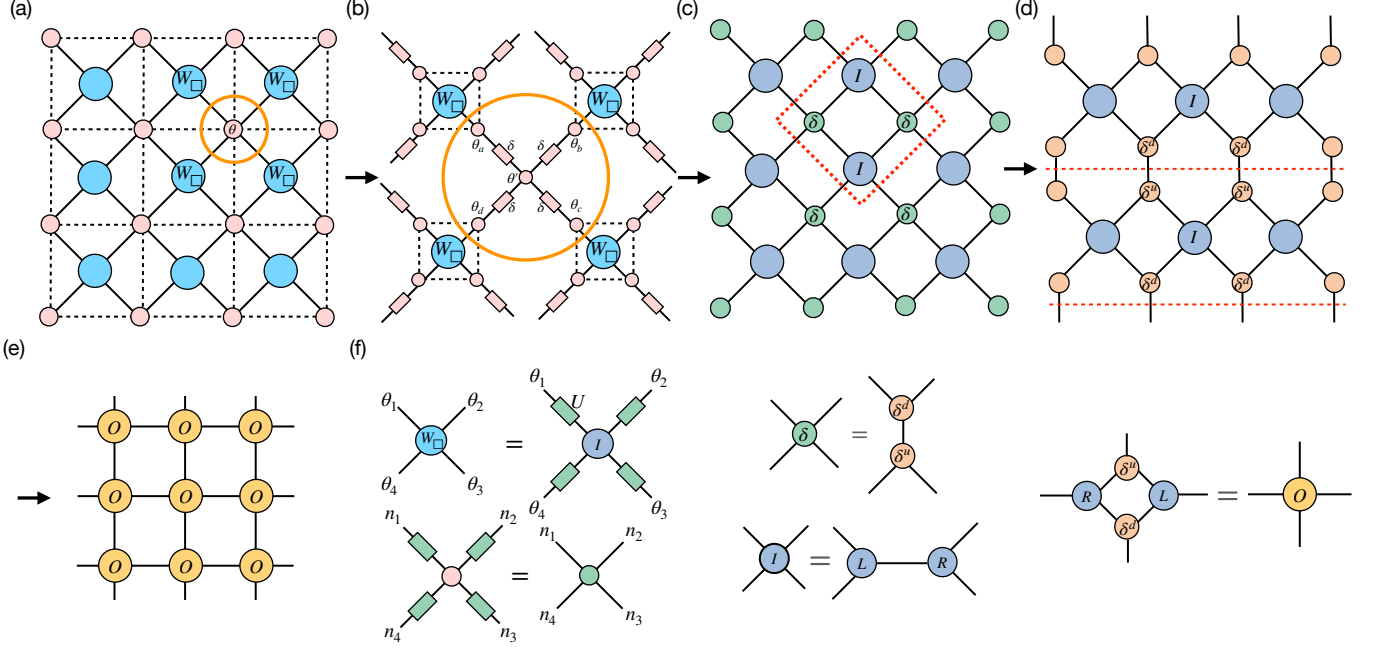


FIG. 8: Tensor network representation of the FFXY model on a square lattice. (a) The tensor network with continuous indices, where the W tensors account for the Boltzmann weight on each square and the pink dot tensor accounts for the integration of the shared θ variables among four plaquettes. The black dotted line denotes the original square lattice. (b) The auxiliary spin θ' connecting the copied spins of four nearby plaquettes, the δ matrices represent the Dirac delta functions. (c) The tensor network with discrete indices obtained from Fourier transformations on the W tensors and the integrations on the θ variables. (d) The row-to-row transfer matrix built by splitting the δ tensors vertically. (e) The uniform tensor network representation composed of local tensor O . (f) The details of the operations on the local tensors in the construction of the tensor network.

into a tessellation of local Hamiltonian on each square where the emergent variables live

$$H = \sum_{\square} H_{\square}, \quad (35)$$

and the local cluster of interactions is given by

$$H_{\square} = -\frac{J}{2} \sum_{\langle i,j \rangle \in \square} \cos(\theta_i - \theta_j - A_{ij}). \quad (36)$$

Then the tensor network can be expressed as a product of local Boltzmann weights on each plaquette as shown in Fig. 8 (a)

$$Z = \prod_i \int \frac{d\theta_i}{2\pi} \prod_{\square} W_{\square} \quad (37)$$

where $W_p(\theta_1, \theta_2, \theta_3, \theta_4) = e^{-\beta H_{\square}}$ is a four-legged tensor with a continuous $U(1)$ indices.

Different from the corner-shared case of the kagome lattice, particular attention should be paid to the split of the shared spins among four square plaquettes. To avoid the formation of loops of the Dirac delta functions among four W tensors

$$\delta(\theta_a - \theta_b)\delta(\theta_b - \theta_c)\delta(\theta_c - \theta_d)\delta(\theta_d - \theta_a)$$

with $\theta_a, \theta_b, \theta_c$ and θ_d representing the four replicas of the shared spin, we put an auxiliary spin θ'_i connecting to the shared spins

$$\delta(\theta_a - \theta')\delta(\theta_b - \theta')\delta(\theta_c - \theta')\delta(\theta_d - \theta')$$

in a star shape as shown in Fig. 8 (b). Then we transform the local tensor W_p to the discrete basis

$$I_{n_1, n_2, n_3, n_4} = \prod_{i=1}^4 \int \frac{d\theta_i}{2\pi} W_{\Delta}(\theta_1, \theta_2, \theta_3, \theta_4) \cdot U_{n_1}(\theta_1)U_{n_2}(\theta_2)U_{n_3}(\theta_3)U_{n_4}(\theta_4), \quad (38)$$

where $U_n(\theta)$ are the Fourier basis defined in (31).

As shown in Fig. 8 (f), the constraint of the star-shaped Dirac delta functions (38) can be reduced to a four-legged Kronecker delta tensor via

$$\delta_{n_1+n_2+n_3+n_4, 0} = \int \frac{d\theta'}{2\pi} U_{n_1}(\theta')U_{n_2}(\theta')U_{n_3}(\theta')U_{n_4}(\theta')$$

characterizing the conservation law of $U(1)$ charges. As a result, we get the tensor network representation composed of local tensors of discrete indices as displayed in Fig. 8 (c).

Furthermore, the δ tensors are split vertically as shown in Fig. 8 (d),

$$\delta_{n_1+n_2+n_3+n_4, 0} = \sum_{n_5} \delta_{n_1+n_2-n_5, 0}^u \delta_{n_3+n_4+n_5, 0}^d \quad (39)$$

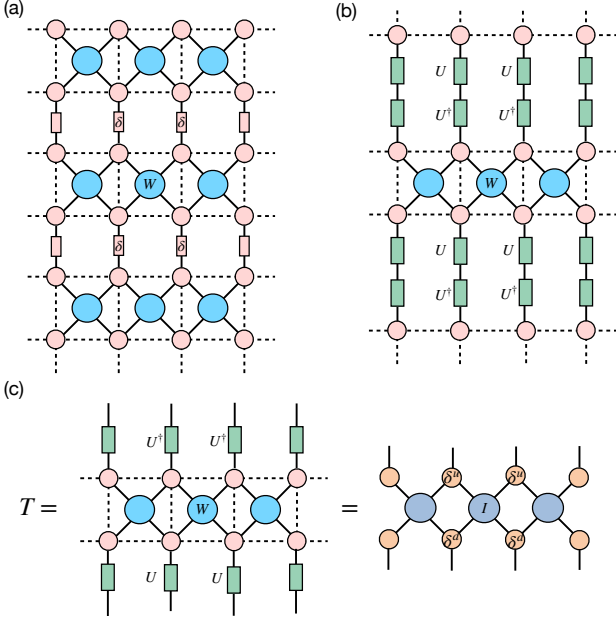


FIG. 9: (a) Tensor network representation of the partition function with the split of $U(1)$ phase variables vertically. The δ matrices represent the Dirac delta functions. (b) The decomposition of the Dirac delta function into U matrix and U^\dagger matrices. (c) The row-to-row transfer matrix on the continuous basis and the discrete basis, respectively.

and the I tensors are decomposed horizontally by SVD

$$I_{n_1, n_2, n_3, n_4} = \sum_{n_5} L_{n_1, n_2, n_5} R_{n_5, n_3, n_4} \quad (40)$$

as displayed in Fig. 8 (f). Finally, the regular local tensor O in the uniform tensor network of Fig. 8 (e) is obtained by grouping the relevant component tensors.

One might rotate the network in Fig. 8 (c) by 45 degrees and group the local tensors in the red dotted line to directly make up a four-legged translation-invariant local tensor. However, the standard contraction algorithms fail to converge under this construction because the linear transfer matrix is non-Hermitian. Another key insight is that such a construction does not take into account the checkerboard-like ground state configurations, where only two chiralities are included in the transitional unit.

Actually, although the procedure of the construction is different, the tensor network in Fig. 8 turns out to share the same transfer matrix as the one obtained in the Ref.²⁴. To prove it, we split the $U(1)$ spins in the vertical direction using the relation

$$\int d\theta_i f(\theta_i) = \iint d\theta_i d\theta'_i \delta(\theta_i - \theta'_i) f(\theta'_i), \quad (41)$$

where the spin θ'_i is a copy of spin θ_i connected by the Dirac delta function as shown in Fig. 9 (a). The delta tensor on a link can be further decomposed by the Fourier

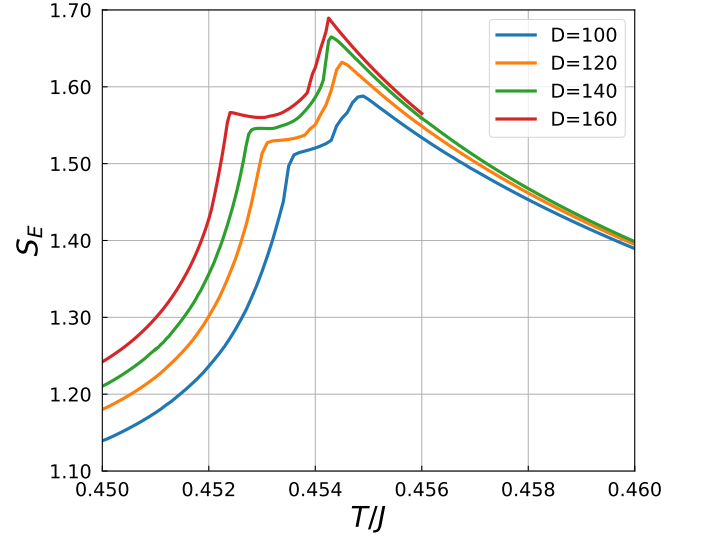


FIG. 10: The entanglement entropy for the FFXY model on the square lattice develops two singularities indicating the existence of two phase transitions with the increasing of MPS bond dimensions.

basis

$$\delta(\theta - \theta') = \frac{1}{2\pi} \sum_n U_n^\dagger(\theta') U_n(\theta), \quad (42)$$

as displayed in Fig. 9 (b). Now we can define the row to row transfer matrix as three stripes of U , W and U^\dagger tensors as shown in Fig. 9 (c). It is easy to see that the transfer matrix is Hermitian just like the one constructed in Ref.²⁴ since the W tensors are real and symmetric. Using the Fourier transformation again, we get the same I and δ tensors in Fig. 9 (c) as those displayed in Fig. 8 (d).

Once the proper tensor network representation is obtained, the numerical calculations can be efficiently performed as illustrated in the Appendix. As shown in Fig. 10, the entanglement entropy S_E develops two sharp singularities at two critical temperatures T_{c1} and T_{c2} , which strongly indicates the existence of two phase transitions at two different temperatures. As the singularity positions vary with the MPS bond dimension D , the critical temperatures T_{c1} and T_{c2} can be determined precisely by extrapolating the bond dimension D to infinite. Moreover, we find that the critical temperatures T_{c1} and T_{c2} exhibit different scaling behaviors in the linear extrapolation, implying that the two phase transitions belong to different kinds of universality classes. The lower transition temperature T_{c1} varies linearly on the inverse square of the logarithm of the bond dimension, while the higher transition temperature T_{c2} has a linear variance with the inverse bond dimension. The different scaling behavior agrees well with the different critical behavior of the BKT and 2D Ising universality classes²⁴.

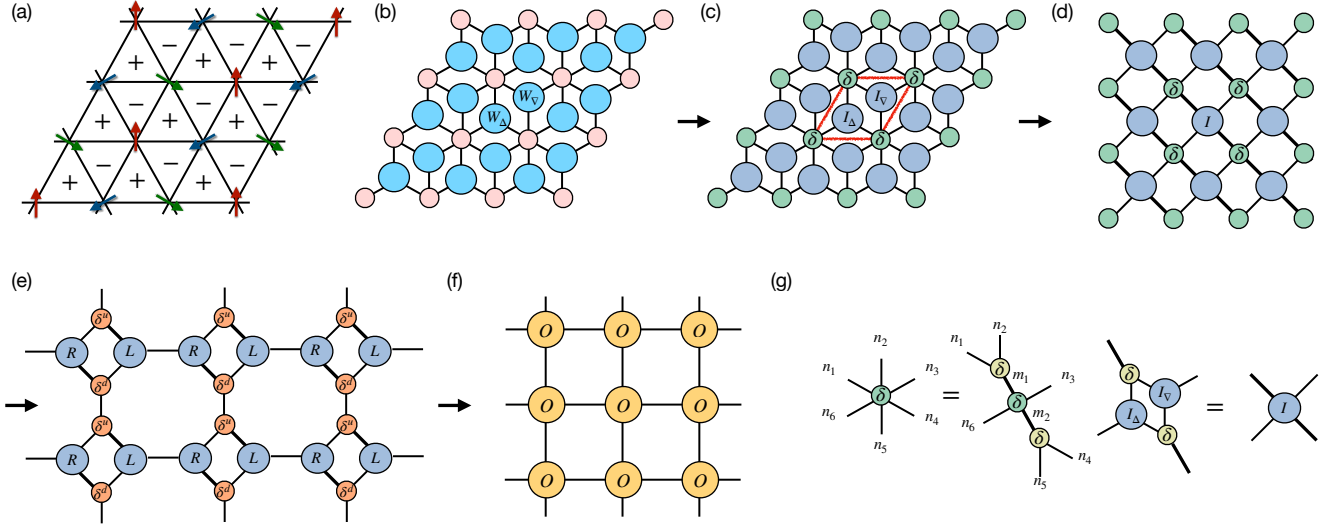


FIG. 11: The tensor network representation of the FFXY model on a triangular lattice. (a) One of the ground state spin configurations. The chiralities denoted by plus and minus signs on the centers of the triangular plaquettes form an AF pattern. (b) The tensor network with continuous indices. (c) The tensor network is transformed onto a discrete basis through the Fourier transformation. A parallelogram unit cell is circled in the red line. (d) The I tensors is constructed by grouping a pair of I_∇ and I_Δ tensors. (e) The vertical split of the δ tensors into δ^d and δ^u and the horizontal split of the I tensors into L and R . (f) The tensor network representation composed of uniform local O tensors. (g) Details of the transformations of local tensors.

D. AF XY spin model on a triangular lattice

The frustrated XY spin model on a triangular lattice under a fixed gauge condition of $A_{ij} = \pi$ on each triangular plaquette can be transformed into an AF XY spin model. As shown in Fig. 11 (a), the angle between each pair of the nearest-neighbor spins should be $\pm 2\pi/3$ to achieve the minimum of the ground state energy. Like the FFXY model on the square lattice, the elementary triangular plaquettes can be characterized by alternating chiralities of $\tau = \pm 1$. The translation-invariant unit of the spin configuration forms a 3×3 cluster larger than the original lattice.

The tensor network can be constructed in the same way as the FFXY spin model on the square lattice. First, we decompose the Hamiltonian into local terms on each triangle

$$H = \sum_p H_p, \quad H_p = \frac{J}{2} \sum_{\langle i,j \rangle \in p} \cos(\theta_i - \theta_j). \quad (43)$$

The partition function can be expressed as a product of local Boltzmann weights

$$Z = \prod_i \int \frac{d\theta_i}{2\pi} \prod_p W_p, \quad (44)$$

where $W_p = e^{-\beta H_p}$ defined on the centers of the triangles are three-legged tensors sharing the same $U(1)$ spin at the joint corners as shown in Fig. 11 (b).

Then the W tensors and the Dirac delta functions are transformed onto a discrete basis by the Fourier trans-

formations, as displayed in Fig. 11 (c). To achieve a transition-invariant unit, we take a parallelogram cell circled by the red line and reorganize the local tensors within it. As shown in Fig. 11 (g), the six-legged delta tensor is decomposed into three smaller delta tensors

$$\begin{aligned} & \delta_{n_1+n_2+n_3+n_4+n_5+n_6,0} \\ &= \sum_{m_1, m_2} \delta_{n_1+n_2, m_1} \delta_{m_1+n_3+m_2+n_6, 0} \delta_{n_4+n_5, m_2}, \end{aligned}$$

where the bond dimension of the m -indexed leg is bigger than the n -indexed leg denoted by a thicker line. At the same time, a pair of I_Δ and I_∇ tensors are grouped together into a four-legged I tensor

$$\begin{aligned} I_{n_1, m_2, n_3, m_4} &= \sum_{n_2, n_4, n_5, n_6} \delta_{n_2+n_4, m_2} \\ & (I_\Delta)_{n_1, n_2, n_5} \delta_{n_5+n_6, m_4} (I_\nabla)_{n_3, n_4, n_6}, \end{aligned}$$

and the tensor network is transformed to a relatively structured form in Fig. 11 (d). Following the same procedure of a vertical split of the δ tensors and a horizontal split of the I tensors, we obtain the uniform tensor network in Fig. 11 (f).

Note that the Fourier transformation must be performed on each triangular plaquette first to ensure the emergence of the dual variables. Otherwise, if we directly choose a parallelogram including a pair of neighboring triangles and then build the tensor network based

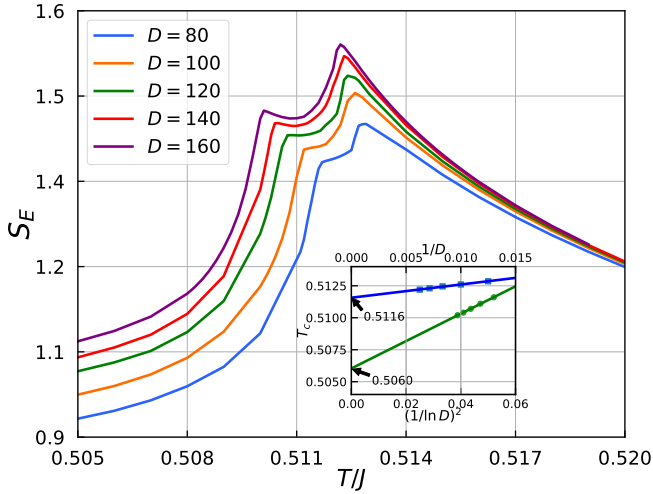


FIG. 12: For the AF XY model on the triangular lattice, the entanglement entropy as a function of temperature develops two peaks when the MPS bond dimension D is increased. Inset: The singularity temperatures T_{c1} and T_{c2} of the entanglement entropy fitted for MPS bond dimensions from $D = 80$ to 160.

on the local Boltzmann weight of

$$\begin{aligned}
 & W_{\square}(\theta_1, \theta_2, \theta_3, \theta_4) \\
 &= \exp \left\{ -\frac{\beta J}{2} [\cos(\theta_1 - \theta_2) + \cos(\theta_2 - \theta_3) \right. \\
 &\quad \left. + \cos(\theta_3 - \theta_4) + \cos(\theta_4 - \theta_1) + 2 \cos(\theta_1 - \theta_3)] \right\},
 \end{aligned}$$

the infinite contraction of the tensor network will not give the right results. The reason is that the construction of local tensors with a finite bond cut-off can be regarded as a coarse-grained procedure that should be performed exactly on the clusters of spin corresponding to the emergent degrees of freedom.

As shown in Fig. 12, the entanglement entropy S_E also develops two sharp singularities at two critical temperatures T_{c1} and T_{c2} , and the critical temperatures have the same scaling behavior as the FFXY model on the square lattice. From the linear extrapolation, the critical temperatures are estimated to be $T_{c1} \simeq 0.5060J$ and $T_{c2} \simeq 0.5116J$. The critical temperature T_{c1} agrees well with previous Monte Carlo results⁶⁶ obtained by BKT fitting and T_{c2} is slightly lower than a recent estimation^{66,67} of $T_{c2} \simeq 0.512J$.

The properties of the two distinct phase transitions can be further elucidated through the thermodynamic quantities. The results of the specific heat are presented in Fig. 13 (a). Around the critical temperature T_{c1} , the specific heat exhibits a small bump, indicating a higher-order continuous phase transition. By comparison, the specific heat displays a sharp divergence at T_{c2} , implying a second-order phase transition. For the high-temperature side $T > T_{c2}$, the specific heat can be fitted well by the logarithmic behavior of a second-order Ising transition.

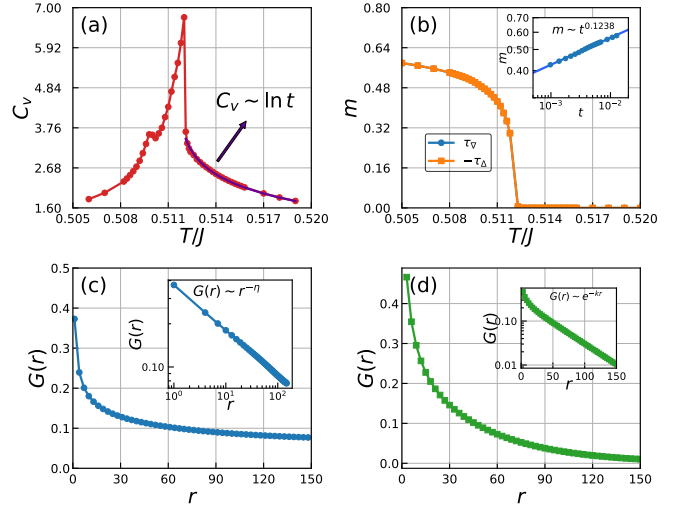


FIG. 13: (a) The specific heat shows a small bump around T_{c1} but a logarithmic divergence at T_{c2} . (b) The symmetry breaking of chirality at T_{c2} . The inset is the fitting of the Ising critical exponent. (c) The spin-spin correlation function shows a power-law decay below T_{c1} (d) The spin-spin correlation function shows an exponential decay above T_{c1} .

The specific heat between T_{c1} and T_{c2} does not fit well with the logarithmic form due to the close proximity of the two transitions. The breaking of Z_2 symmetry at T_{c2} can be demonstrated by the expectation values of the chiralities. As shown in Fig. 13 (b), below the critical temperature T_{c2} , the chiral order parameter

$$m = \frac{1}{N} \sum_p (-1)^{x+y} \tau_p \quad (45)$$

associated with the chiral degrees of freedom establishes a non-zero value, corresponding to the checkerboard pattern of chirality on upward and downward triangles. When approaching the critical temperature T_{c2} from the low-temperature side, the order parameter vanishes continuously as $m \sim t^\beta$ with $t = 1 - T/T_{c2}$. The critical exponent $\beta \simeq 0.1238$ is in good agreement with the critical exponent $\beta = 1/8$ for the 2D Ising universality class.

The nature of the phase transition at T_{c1} can be revealed in the change of the behavior of the spin-spin correlation functions defined as

$$G(r) = \langle \cos(\theta_i - \theta_{i+r}) \rangle. \quad (46)$$

A comparison of correlation functions below and above T_{c1} is displayed in Fig. 13(c) and (d). Below T_{c1} , the spin-spin correlation function exhibits a power-law decay, implying a close binding between vortices and anti-vortices. In contrast, for $T > T_{c1}$ the correlation function displays an exponential decay, indicating the destruction of phase coherence between vortices due to the unbinding of vortex pairs. Thus, the phase transition at T_{c1} belongs to the universality class of the BKT transition.

E. Modified XY model on a square lattice

The unified tensor network methods can be employed in the study of frustrated spin models with more complex interactions. One such model is the modified XY model defined on a 2D square lattice^{68,69}

$$H = -J \sum_{\langle i,j \rangle} \cos(\theta_i - \theta_j) - \mu \sum_p \tau_p^2, \quad (47)$$

where the first term is the original XY model of ferromagnetic coupling $J > 0$, and the second term tunes the vortex fugacity through the chemical potential μ . The spin current circulating around each single square plaquette is defined as

$$\tau_p = \sum_{\langle i,j \rangle \in p} \sin(\theta_i - \theta_j).$$

It is well-known that the original XY spin model can be mapped into an interacting Coulomb gas with a vortex-core energy fixed in the low-density limit^{61,62}. And the underlying physics at large vortex density is of general interest both theoretically and experimentally. In the area of theoretical investigations, the possible extension of BKT theory under a large vortex fugacity was discussed, where non-BKT behavior and the occurrence of first-order transition were proposed^{63,70-72}. Actually a generalization of 2D XY spin model with a "crossed-product" operator acting on the plaquettes had been introduced to adjust the core energy of the vortices⁷³. Subsequently, the numerical explorations of a Coulomb gas model on the square and triangular lattices as well as in the continuous limit showed a rich phase diagram with novel critical behaviors of an ordered-charge lattice⁷⁴⁻⁷⁶. Moreover, the similar physics has been investigated in 3D XY spin models, where a term acting on the plaquette was introduced to regulate the energy of vortex strings^{77,78}.

The experiments in superconducting thin films revealed a significant deviation of the vortex-core energy from the predictions in the original XY model⁷⁹. It was found that an accurate consideration of the vortex-core energy is of great importance for the experimental identification of the BKT transition⁸⁰. Apart from the widely known superfluid phase and normal phase, the measurement of the third sound mode in ⁴He thin films suggested the existence of a new phase⁸¹. To provide a theoretical explanation for this phenomenon, researchers have proposed a fascinating concept involving the formation of a lattice composed of vortices and anti-vortices, with a remarkably low vortex core energy^{82,83}. The existence of vortex-antivortex lattice has also been proposed in other systems such as ultra-cold atoms⁸⁴ and polariton fluids⁸⁵.

To understand the role of the modified interaction term τ_p , we can make a simple analysis of the ground state. The ground state structure can be determined by the ratio of μ/J tuning the spin currents in the system which effectively modulates the vortex fugacity. As illustrated

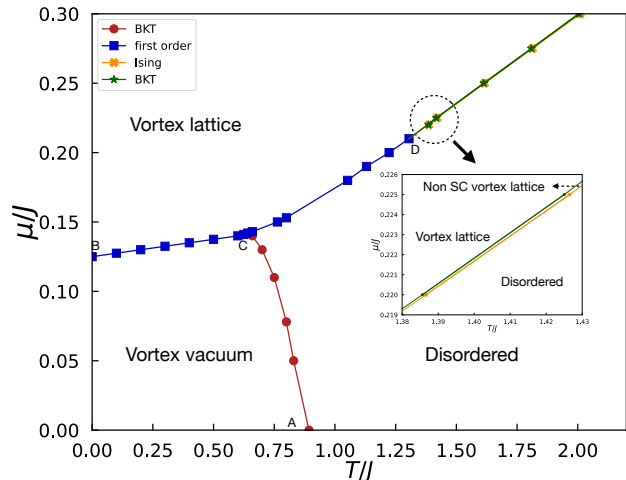


FIG. 14: The global phase diagram of the modified XY spin model. The BKT transition point A of the original XY spin model is determined as $(0.893, 0)$. The exact solvable point B between the vortex vacuum phase and vortex lattice phase at zero temperature is given by $(0, 0.125)$. As the temperature increases, depending on the chemical potential, the vortex lattice can melt through three possible way. Below the point C at $(0.64, 0.142)$, the vortex lattice experiences a first-order transition into the vortex vacuum phase and then undergoes a BKT transition into the disordered phase, while the CD line is the first-order transition. The point D is a tricritical point determined as $\mu/J \simeq 0.21$. Above this point D, the first order transition line is separated into two extremely close transition lines, belonging to the BKT transition and Ising transition, respectively. Inset shows the enlarged results around the point D.

in Fig. 7(c)-(d), when $\mu/J < 1/8$, the ground state is identical to that at $\mu = 0$, corresponding to the ground state of the original XY model where all spins align parallel to each other. As we further increase the chemical potential to $\mu/J > 1/8$, the ground state is characterized by maximizing τ_p on each plaquette, resulting in a phase difference of $\phi_{12} = \phi_{23} = \phi_{34} = \phi_{41} = \pm\pi/2$. This ground state has the same ground state degeneracy as the FFX spin model on a square lattice. From the perspective of vorticity, the ground state at $\mu/J < 1/8$ has zero vorticity at each plaquette termed as the vortex vacuum state, whereas the ground state at $\mu/J > 1/8$ has a checkerboard pattern of vorticity equal to ± 1 called the vortex-antivortex crystal. Hence, the zero-temperature ground state structure of the modified XY spin model is analogous to the 2D dense coulomb gas on the square lattice⁷⁴.

The square term τ_p^2 gives rise to multiple types of interaction including the nearest-neighbor interactions, next-nearest-neighbor interactions, and four-body interactions. Although it seems difficult to treat the four-body interactions, there is still a well-defined vorticity on each plaquette from the viewpoint of emergent degrees of freedom. Therefore we can choose each square plaquette as

an elementary cluster and replace the H_p and W_p by

$$H_p = -\frac{J}{2} \sum_{\langle i,j \rangle \in p} \cos(\theta_i - \theta_j) - \mu \tau_p^2, \quad W_p = e^{-\beta H_p}. \quad (48)$$

Then the tensor network of the partition function can be constructed following the procedure outlined in Fig. 8. The singular behavior of the entanglement entropy corresponding to the 1D transfer operator offers a sharp criterion to determine all possible phase transitions in the thermodynamic limit and the complete phase diagram is thus determined as presented in Fig. 14.

In the upper plane of the phase diagram, the entanglement entropy along the chemical potential $\mu = 0.3J$ is displayed in Fig. 15 (a). There exist two distinct peaks, corresponding to the BKT and Ising transition, respectively. These two phase transitions are extremely close to each other as shown by the zoomed inset in Fig. 14. Upon further reducing the chemical potential to $\mu \simeq 0.20J$, two separated peaks merge into a single peak, as displayed in Fig. 15 (b). The merging point is denoted as the point D in the global phase diagram. The low-temperature phase with large μ is called the vortex-lattice phase due to the checkerboard pattern of vortices and anti-vortices coexisting with the SC order. The chiral LRO is demonstrated by the finite expectation value of chiralities (45) as shown in Fig. 16 (b) and Fig. 17 (b). The SC order is characterized by the quasi-LRO of $U(1)$ spins, where the spin-spin correlation function (46) displays a power-law decay as displayed in Fig. 16 (d). The melting of the vortex lattice undergoes two steps into the disordered phase with an intermediate non-SC vortex-lattice phase. In the non-SC vortex-lattice phase, the chiral LRO survives but the phase coherence between vortices is destroyed. Such a two-step procedure has been extensively investigated in the FFX models^{24,41,65}.

Below the point D , the phase boundaries are determined by a combined analysis of the entanglement entropy and free energy. We find that the fixed-point equations have two different solutions across the critical point depending on the initial states we start from. The proper solution is chosen with a lower free energy density. As shown in Fig. 15 (c), along the line $T = 0.8J$, the entanglement entropy exhibits a peak at $\mu \simeq 0.080J$ corresponding to the BKT transition and a discontinuous jump at $\mu \simeq 0.153J$ associated to a first-order phase transition. The free energy density of Fig. 15 (e) displays an inflection point of a first-order transition at $\mu \simeq 0.153J$, demonstrating that the entanglement entropy can serve as a powerful criterion for the determination of the first-order phase transition. Besides, we find that the position of the first-order transition is nearly unchanged with increasing bond dimensions, in good agreement with the behavior of the entanglement entropy. As the temperature decreases, the BKT transition line CA and the first-order transition line CD become closer and finally merge into a single first-order transition line CB at the tricritical point C with $T \simeq 0.640J$ and $\mu \simeq 0.142J$. As shown

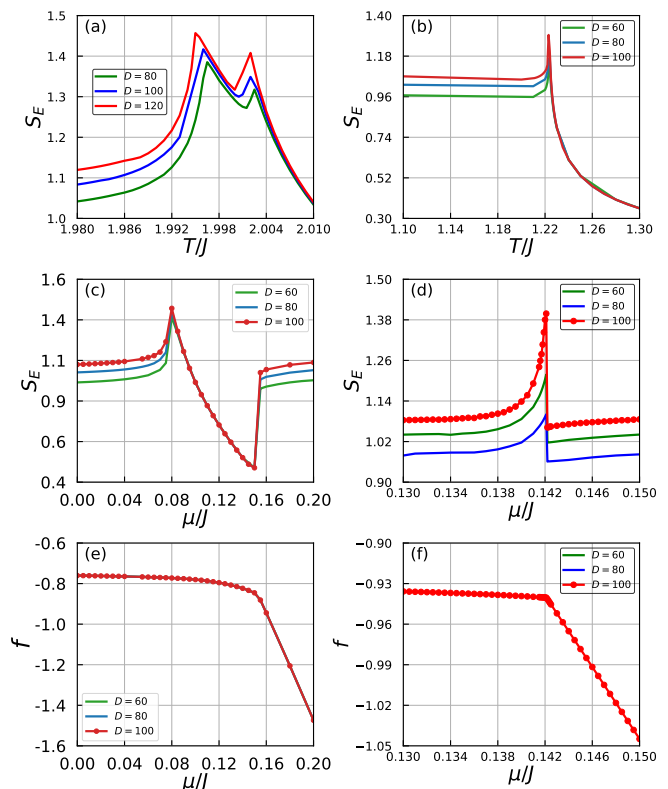


FIG. 15: (a) The entanglement entropy as a function of temperature along $\mu = 0.3J$. (b) The entanglement entropy as a function of temperature along $\mu \simeq 0.20J$. (c) The entanglement entropy as a function of chemical potential along $T = 0.8J$. (d) The entanglement entropy as a function of chemical potential along $T = 0.64J$. (e) The free energy density as a function of chemical potential along $T = 0.8J$. (f) The free energy density as a function of chemical potential along $T = 0.64J$.

in Fig. 15 (d), along the line $T = 0.64J$, the entanglement entropy shows a discontinuous jump just above the peak position of $\mu \simeq 0.142J$. The corresponding free energy density is displayed in Fig. 15 (f) with an evident cusp point.

Across the transition line CD , the vortex lattice melts directly into the disordered phase via a first-order transition, where the chiral LRO and spin quasi-LRO break down simultaneously. As is shown in Fig. 17 (a) and (b), both the thermal entropy density S and the chiral order parameter m develop a discontinuous jump at the transition point of $\mu \simeq 0.18$ and $T \simeq 1.052$. A comparison between the spin-spin correlation functions across the line CD is displayed in Fig. 17 (c) and (d). For a given temperature of $T = 1.05J$ in the vortex-lattice phase, the correlation function $G(r)$ displays a power-law behavior. But in the disordered phase with $T = 1.06J$, the correlation function behaves in an exponential way. We should point out that the existence of a novel continuous transition arising from the merging of BKT and Ising transitions⁸⁶⁻⁹⁰ is not found here.

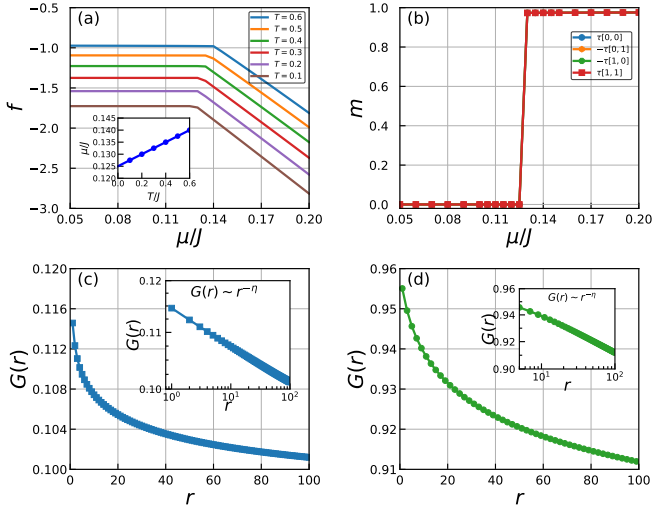


FIG. 16: (a) The free energy density as a function of chemical potential at different temperatures. Inset: linear extrapolation of critical chemical potential as a function of temperature. (b) The checkboard-like chirality pattern along $T = 0.1J$. (c) The spin-spin correlation function shows an exponential decay at $T \simeq 0.1J$ and $\mu \simeq 0.1J$ in the vortex-vacuum phase. (d) The spin-spin correlation function shows a power-law decay at $T \simeq 0.1J$ and $\mu \simeq 0.15J$ in the vortex-lattice phase.

At low temperatures, the phase boundary CB belongs to a first-order transition between the vortex-lattice phase and the vortex-vacuum phase. As shown in Fig. 16(b), when going down along $T = 0.1J$ line, the chiral order parameter m exhibits a discontinuous jump to zero at $\mu \simeq 0.128J$. Since the vortex fugacity is greatly suppressed by decreasing the chemical potential μ , the vortex density drops dramatically, driving the system into the vortex-vacuum phase. Note that the “vortex vacuum” just means that there is no excitation of free vortices but the charge-neutral vortex-antivortex pairs can still be excited. The excitation of vortex-antivortex pairs destroys the LRO of the $U(1)$ spins and gives rise to the well-known BKT quasi-LRO state. As can be seen in Fig. 16 (c)-(d), the spin-spin correlation function displays a power-law decay in both the vortex-lattice and vortex-vacuum phases. When the temperature further decreases, the first-order transition line CB behaves in a linear way. Such a linear behavior is displayed in Fig. 16 (a), where the extrapolation to the zero temperature gives $\mu = 0.125J$ in the inset. The terminal point B is determined at $T = 0$ and $\mu = 0.125J$, consistent with our previous analysis of the ground state.

Finally, the transition line CA separating the vortex-vacuum and disordered phase is the conventional BKT transition, driven by the dissociation of vortex-antivortex pairs. The inverse process, when the system is cooling from a disordered phase, pairs of vortex and anti-vortex appear and further condensed into a square vortex lattice is analogous to the theoretical proposal in ultracold

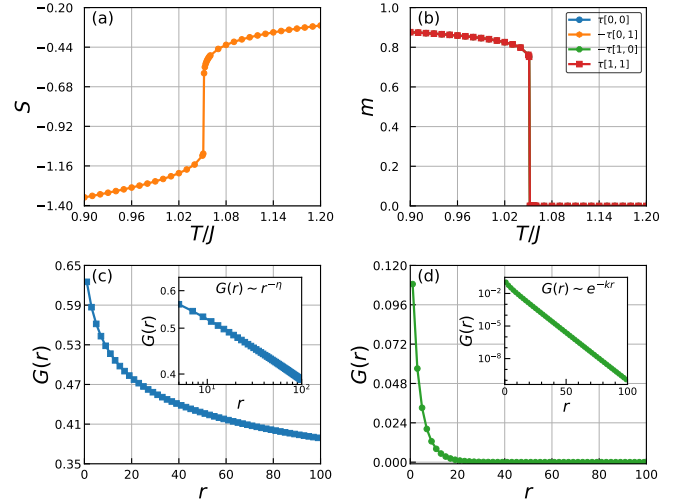


FIG. 17: (a) The thermal entropy density as a function of temperature along $\mu = 0.18J$. (b) The chirality on 2×2 sublattice as a function of temperature along $\mu = 0.18J$. (c) The spin-spin correlation function at $T \simeq 1.05J$, and $\mu \simeq 0.18J$ in vortex lattice phase shows a power-law decay. (d) The spin-spin correlation function at $T \simeq 1.06J$ and $\mu \simeq 0.18J$ in disordered phase displays an exponential decay.

Fermi gases⁸⁴. The rich phase diagram of the modified XY model provides important insights into the formation of the vortex lattice and the complex melting process. By tuning the vortex chemical potential, the unconventional phase transitions in SC lattice are investigated thoroughly in the orientational $U(1)$ phase variables. A more comprehensive study should take into account the positional order since the vortex lattice may also melt via the Kosterlitz-Thouless-Halperin-Nelson-Young procedure^{82–84,91–93}.

IV. DISCUSSION AND OUTLOOK

In this paper, we have developed a generic tensor network approach to study the frustrated classical spin models with both discrete and continuous degrees of freedom on a wide range of 2D lattices. The key point for a contractible tensor network representation of the partition function is that the emergent degrees of freedom induced by frustrations should be encoded in the local tensors comprising the infinite network. In this way, the massive degeneracy can be described by the interactions between emergent dual variables representing a cluster of interacting spins under the constraint of frustrations. We showed that a common process can be applied to the construction of the tensor network based on ideas of emergent degrees of freedom and duality transformations. We demonstrated the power of our method by applying it to a large array of classical frustrated Ising models and fully frustrated XY spin models on the kagome, triangular and square lattices in the whole temperature range.

Our tensor network approach turned out to be a natural generalization of the previous solutions of frustrated spin systems^{24,40,48,49} but from a more fundamental basis. Then the partition function is expressed in terms of a product of 1D transfer matrix operator, whose eigen equation was solved by the algorithms based on matrix product states rigorously. The singularity of the entanglement entropy for the 1D quantum analog provides a stringent criterion to determine various phase transitions with high accuracy. Apart from the good agreement with previous findings, our numerical results offer new clarification of the phase structure of the AF triangular XY model and the modified XY model.

The generic tensor network approach provides a promising way to deal with some remaining open questions on frustrated systems. First, our method should be applicable to frustrated spin models with longer-range interactions where emergent degrees of freedom play an important role in characterizing the collective behavior. For example, a range of novel classical spin liquid phase in the J_1 - J_2 - J_3 Ising model at the fine-tune point can be understood by topological charges with the nearest neighbor interaction and hence can be solved directly from our tensor network approach⁹⁴⁻⁹⁶. Second, the long-standing problems in uniform frustrated XY spin models may be solved by our generic construction. All the frustration ratio $f \in [0, 1]$ can be represented by a suitable gauge field on the lattice bond, which can be further represented using the standard procedure. Finally, we should point out that our construction should be extended to other models in any dimension with emergent degrees of freedom. For instance, the classical Heisenberg antiferromagnet^{97,98} may be investigated in the future where the basis for the dual transformation should be spherical harmonic functions. We believe that further development of the tensor network approach of our work should lead to the solution of a number of problems in frustrated systems that were difficult to solve previously.

Acknowledgments

The authors are very grateful to Tao Xiang for his stimulating discussions. The research is supported by the National Key Research and Development Program of MOST of China (2017YFA0302902).

Appendix: Tensor network calculations of the physical quantities

1. Linear transfer matrix method

Once the proper tensor network representations for the frustrated models are obtained, the contraction of the infinite tensor network can be performed efficiently. One of the best practices to contract a translation-invariant

tensor network in the thermodynamic limit is the algorithm of uniform matrix product states where the leading eigenvector of the row-to-row transfer matrix is calculated using a set of optimized eigensolvers^{52,53,60}.

Due to the emergent phenomena in the frustrated systems, the lattice symmetry is usually spontaneously broken with a larger translation-invariant unit composed of new degrees of freedom. The relevant 2D tensor network should consist of a larger unit cell of multiple tensors that matches the transitional symmetry. For example, a 2×2 plaquette structure of O tensors is necessary to represent the checkerboard ground state of the FFX model on square lattices and a 3×3 structure for the triangular AF XY model.

The fixed-point equation for the enlarged transfer operator can be accurately solved by the multiple lattice-site VUMPS algorithm with only a linear growth in computational cost⁵⁴. For a transition-invariant cluster consisting of $n_x \times n_y$ local tensors, the whole transfer matrix is formed by y rows of linear transfer matrices

$$\mathcal{T} = T^{(y+n_y-1)} \dots T^{(y)}, \quad (\text{A.1})$$

where each row of the component transfer matrix is defined by

$$T^{(y)} = \text{tTr} \left(\dots O^{(x,y)} O^{(x+1,y)} \dots \right) \quad (\text{A.2})$$

with $x = 0, \dots, n_x - 1$, and $y = 0, \dots, n_y - 1$. The transfer operator \mathcal{T} can be regarded as the matrix product operator (MPO) for the 1D quantum spin chain, whose logarithmic form can be mapped to a 1D quantum system with complicated spin-spin interactions

$$\hat{H}_{1D} = -\frac{1}{\beta} \ln \mathcal{T}. \quad (\text{A.3})$$

In this way, the correspondence between the finite temperature 2D statistical model and the 1D quantum model at zero temperature is established.

The eigenequation can be expressed as

$$\mathcal{T}|\Psi(A)\rangle^{(y)} = \Lambda_{\max}|\Psi(A)\rangle^{(y)}, \quad (\text{A.4})$$

where $|\Psi(A)\rangle^{(y)}$ is the leading eigenvector represented by matrix product states (MPS) made up of a n_x -site unit cell of local A tensors with auxiliary bond dimension D

$$|\Psi(A)\rangle^{(y)} = \sum_x \text{Tr}(\dots A^{i(x,y)} A^{i(x+1,y)} \dots) |\dots i_{(x,y)} \dots\rangle \quad (\text{A.5})$$

satisfying $A^{(x,y)} = A^{(x,y+n_y)} = A^{(x+n_x,y)}$ ⁵². The big eigenequation can be further decomposed into a set of smaller eigen-equations displayed in Fig. 18 (a) as

$$T^{(y)}|\Psi(A)\rangle^{(y)} = \Lambda_y|\Psi(A)\rangle^{(y+1)}, \quad (\text{A.6})$$

with a total eigenvalue

$$\Lambda_{\max} = \prod_{y=0}^{n_y-1} \Lambda_y. \quad (\text{A.7})$$

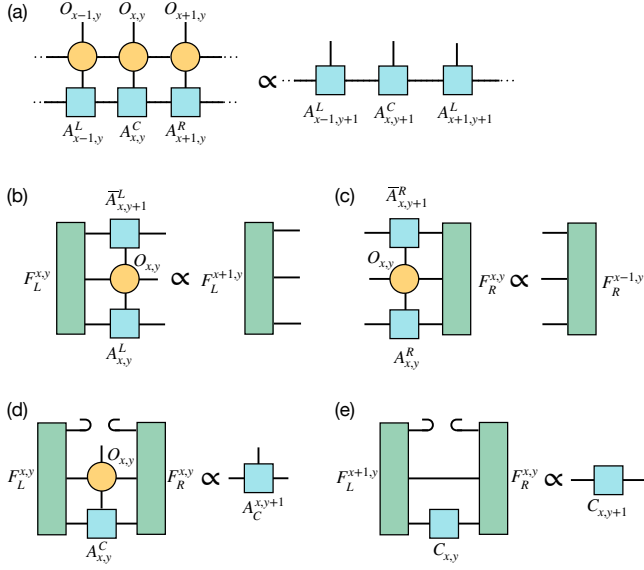


FIG. 18: The key steps of the multi-site VUMPS algorithm. (b) and (c) Eigen-equations to update the left and right environmental fixed points of the channel operators. (e) and (f) Eigen-equations to update the central tensors based on the new environment.

The key process of the algorithm is summarized in Figs. 18 (b)-(e), including sequentially solving the left and right fixed points of the channel operators

$$\mathbb{T}_L^{(x,y)} F_L^{(x,y)} = \lambda_{(x,y)} F_L^{(x+1,y)}, \quad (\text{A.8})$$

$$\mathbb{T}_R^{(x,y)} F_R^{(x,y)} = \lambda_{(x,y)} F_R^{(x-1,y)}, \quad (\text{A.9})$$

and the updating of the central tensors

$$H_{A_C}^{(x,y)} A_C^{(x,y)} = \lambda A_C^{(x,y+1)}, \quad (\text{A.10})$$

$$H_C^{(x,y)} C^{(x,y)} = C^{(x,y+1)}. \quad (\text{A.11})$$

Note that, when solving the fixed point eigen equation (A.8)-(A.11), one may not directly use the linear transfer matrix composed by the uniform local tensor O , but the interior structure should be explored. This will significantly reduce the computational complexity.

2. Physical quantities

From the fixed-point MPS for the 1D quantum transfer operator, various physical quantities can be estimated accurately. The entanglement properties can be detected via the Schmidt decomposition of $|\Psi(A)\rangle^{(y)}$ which bipartites the relevant 1D quantum state of the MPO, and the entanglement entropy can be determined directly from the singular values s_α as

$$S_E = - \sum_{\alpha=1}^D s_\alpha^2 \ln s_\alpha^2, \quad (\text{A.12})$$

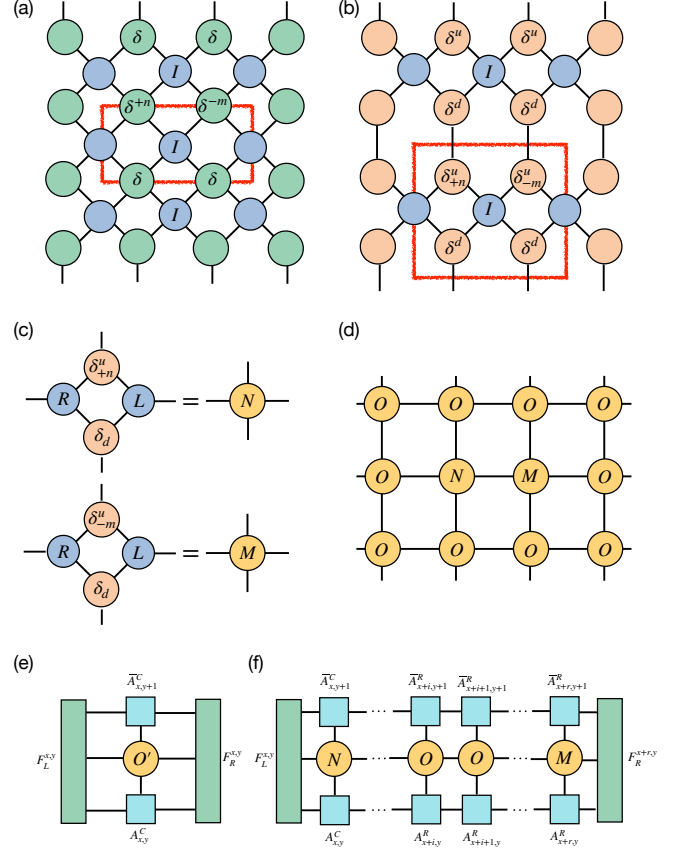


FIG. 19: (a) The imbalanced delta tensors as a result of imbalanced currents introduced by the local observables. (b) The vertical split of the imbalanced delta tensors. (c) The construction of the impurity tensors from imbalanced delta tensors. (d) Two impurity tensors are introduced into the original tensor network. (e) Expectation of a local observable by contracting the leading eigenvectors of the channel operators. (f) Two-point correlation functions calculated by contracting a sequence of channel operators.

in correspondence to the quantum entanglement measure.

Moreover, the expectation value of a local observable can be evaluated by inserting the corresponding impurity tensor into the original tensor network for the partition function. The impurity tensors can be obtained simply by introducing an unbalanced delta tensor to replace the original delta tensor characterizing the constraints of sharing spins.

For Ising spins, the expectation value of a local spin at site j can be expressed as

$$\langle s_j \rangle = \frac{1}{Z} \sum_{\{s_i = \pm 1\}} e^{-\beta E(\{s_i\})} s_j \quad (\text{A.13})$$

where $E(\{s_i\})$ is the energy of a state under a given spin configuration $\{s_i\}$. The s_j term just changes the Kro-

necker delta tensor from the form of (16) to

$$\delta_{s_1, s_2, \dots, s_n} = \begin{cases} s_1, & s_1 = s_2 = \dots = s_n \\ 0, & \text{otherwise} \end{cases}. \quad (\text{A.14})$$

For XY spins, the expectation value of $e^{iq\theta}$ can be calculated by introducing imbalanced currents into the original delta tensors from the conservation form of (39) to

$$\delta^q = \delta_{n_1+n_2+n_3+n_4+q,0} \quad (\text{A.15})$$

as displayed in Fig. 19 (a). Accordingly, the vertical splitting of the delta tensor in (39) should be modified to

$$\delta_{n_1+n_2+n_3+n_4+q,0} = \sum_{n_5} \delta_{n_1+n_2-n_5,0}^u \delta_{n_1+n_2+n_5+q,0}^d \quad (\text{A.16})$$

as shown in Fig. 19 (b). Then the impurity tensors can be constructed in the same way by including the imbalanced delta tensors as depicted in Fig. 19 (c). The tensor

network containing two impurity tensors is displayed in Fig. 19 (d) as an example.

Using the MPS fixed point, the contraction of the tensor network containing the impurity tensor is reduced to a trace of an infinite sequence of channel operators, which can be further squeezed into a contraction of a small network. As shown in Fig. 19 (e), the evaluation of a single variable is expressed as a contraction of only five tensors. And the expectation value of the two-point correlation function

$$G(r) = \langle \cos(n\theta_i - m\theta_{i+r}) \rangle \quad (\text{A.17})$$

can be reduced to a trace of a row of channel operators containing two impurity tensors as shown in Fig. 19 (f).

* These authors contributed equally.

† Electronic address: gmzhang@tsinghua.edu.cn

¹ C. Lacroix, P. Mendels, and F. Mila, *Introduction to Frustrated Magnetism: Materials, Experiments, Theory*, Springer Series in Solid-State Sciences (Springer Berlin Heidelberg, 2011), ISBN 9783642105890, URL <https://books.google.com/books?id=utSV09Zuh0kC>.

² A. P. Ramirez, Annual Review of Materials Science **24**, 453 (1994), <https://doi.org/10.1146/annurev.ms.24.080194.002321>, URL <https://doi.org/10.1146/annurev.ms.24.080194.002321>.

³ R. Moessner, Canadian Journal of Physics **79**, 1283 (2001), <https://doi.org/10.1139/p01-123>, URL <https://doi.org/10.1139/p01-123>.

⁴ H. T. Diep, *Frustrated Spin Systems* (WORLD SCIENTIFIC, 2020), 3rd ed., <https://www.worldscientific.com/doi/pdf/10.1142/11660>, URL <https://www.worldscientific.com/doi/abs/10.1142/11660>.

⁵ A. Ortiz-Ambriz, C. Nisoli, C. Reichhardt, C. J. O. Reichhardt, and P. Tierno, Rev. Mod. Phys. **91**, 041003 (2019), URL <https://link.aps.org/doi/10.1103/RevModPhys.91.041003>.

⁶ J.-F. Sadoc and R. Mosseri, *Introduction to geometrical frustration* (Cambridge University Press, 1999), p. 1–13, Collection Alea-Saclay: Monographs and Texts in Statistical Physics.

⁷ G. H. Wannier, Phys. Rev. **79**, 357 (1950), URL <https://link.aps.org/doi/10.1103/PhysRev.79.357>.

⁸ K. Kanō and S. Naya, Progress of Theoretical Physics **10**, 158 (1953), ISSN 0033-068X, <https://academic.oup.com/ptp/article-pdf/10/2/158/5229090/10-2-158.pdf>, URL <https://doi.org/10.1143/ptp/10.2.158>.

⁹ S. Teitel and C. Jayaprakash, Phys. Rev. B **27**, 598 (1983), URL <https://link.aps.org/doi/10.1103/PhysRevB.27.598>.

PhysRevB.27.598.

¹⁰ J. M. Thijssen and H. J. F. Knops, Phys. Rev. B **42**, 2438 (1990), URL <https://link.aps.org/doi/10.1103/PhysRevB.42.2438>.

¹¹ G. Ramirez-Santiago and J. V. José, Phys. Rev. Lett. **68**, 1224 (1992), URL <https://link.aps.org/doi/10.1103/PhysRevLett.68.1224>.

¹² E. Granato and M. P. Nightingale, Phys. Rev. B **48**, 7438 (1993), URL <https://link.aps.org/doi/10.1103/PhysRevB.48.7438>.

¹³ J.-R. Lee, Phys. Rev. B **49**, 3317 (1994), URL <https://link.aps.org/doi/10.1103/PhysRevB.49.3317>.

¹⁴ S. Lee and K.-C. Lee, Phys. Rev. B **49**, 15184 (1994), URL <https://link.aps.org/doi/10.1103/PhysRevB.49.15184>.

¹⁵ G. Ramirez-Santiago and J. V. José, Phys. Rev. B **49**, 9567 (1994), URL <https://link.aps.org/doi/10.1103/PhysRevB.49.9567>.

¹⁶ P. Olsson, Phys. Rev. Lett. **75**, 2758 (1995), URL <https://link.aps.org/doi/10.1103/PhysRevLett.75.2758>.

¹⁷ V. Cataudella and M. Nicodemi, Physica A: Statistical Mechanics and its Applications **233**, 293 (1996), ISSN 0378-4371, URL <https://www.sciencedirect.com/science/article/pii/S0378437196002105>.

¹⁸ P. Olsson, Phys. Rev. B **55**, 3585 (1997), URL <https://link.aps.org/doi/10.1103/PhysRevB.55.3585>.

¹⁹ E. H. Boubekeur and H. T. Diep, Phys. Rev. B **58**, 5163 (1998), URL <https://link.aps.org/doi/10.1103/PhysRevB.58.5163>.

²⁰ M. Hasenbusch, A. Pelissetto, and E. Vicari, J. Stat. Mech. **2005**, P12002 (2005), URL <https://doi.org/10.1088/1742-5468/2005/12/p12002>.

²¹ S. Okumura, H. Yoshino, and H. Kawamura, Phys. Rev. B **83**, 094429 (2011), URL <https://link.aps.org/doi/10.1103/PhysRevB.83.094429>.

²² Z. Nussinov, Journal of Statistical Mechanics: Theory and Experiment **2014**, P02012 (2014), URL <https://doi.org/10.1088/1742-5468/2014/02/P02012>.

- org/10.1088/1742-5468/2014/02/p02012.
- 23 A. B. Lima, L. A. S. Mól, and B. V. Costa, *Journal of Statistical Physics* **175**, 960 (2019), URL <https://doi.org/10.1007/s10955-019-02271-x>.
 - 24 F.-F. Song and G.-M. Zhang, *Phys. Rev. B* **105**, 134516 (2022), URL <https://link.aps.org/doi/10.1103/PhysRevB.105.134516>.
 - 25 S. Miyashita and H. Shiba, *Journal of the Physical Society of Japan* **53**, 1145 (1984), <https://doi.org/10.1143/JPSJ.53.1145>, URL <https://doi.org/10.1143/JPSJ.53.1145>.
 - 26 W. Y. Shih and D. Stroud, *Phys. Rev. B* **30**, 6774 (1984), URL <https://link.aps.org/doi/10.1103/PhysRevB.30.6774>.
 - 27 D. H. Lee, J. D. Joannopoulos, J. W. Negele, and D. P. Landau, *Phys. Rev. Lett.* **52**, 433 (1984), URL <https://link.aps.org/doi/10.1103/PhysRevLett.52.433>.
 - 28 D. H. Lee, J. D. Joannopoulos, J. W. Negele, and D. P. Landau, *Phys. Rev. B* **33**, 450 (1986), URL <https://link.aps.org/doi/10.1103/PhysRevB.33.450>.
 - 29 S. E. Korshunov and G. V. Uimin, *Journal of Statistical Physics* **43**, 1 (1986), URL <https://doi.org/10.1007/BF01010569>.
 - 30 J. E. Van Himbergen, *Phys. Rev. B* **33**, 7857 (1986), URL <https://link.aps.org/doi/10.1103/PhysRevB.33.7857>.
 - 31 H.-J. Xu and B. W. Southern, *J. Phys. A: Math. Gen.* **29**, L133 (1996), URL <https://doi.org/10.1088/0305-4470/29/5/009>.
 - 32 S. Lee and K.-C. Lee, *Phys. Rev. B* **57**, 8472 (1998), URL <https://link.aps.org/doi/10.1103/PhysRevB.57.8472>.
 - 33 L. Capriotti, R. Vaia, A. Cuccoli, and V. Tognetti, *Phys. Rev. B* **58**, 273 (1998), URL <https://link.aps.org/doi/10.1103/PhysRevB.58.273>.
 - 34 A. B. Harris, C. Kallin, and A. J. Berlinsky, *Phys. Rev. B* **45**, 2899 (1992), URL <https://link.aps.org/doi/10.1103/PhysRevB.45.2899>.
 - 35 M. S. Rzchowski, *Phys. Rev. B* **55**, 11745 (1997), URL <https://link.aps.org/doi/10.1103/PhysRevB.55.11745>.
 - 36 V. B. Cherepanov, I. V. Kolokolov, and E. V. Podivilov, *Journal of Experimental and Theoretical Physics Letters* **74**, 596 (2001), URL <https://doi.org/10.1134/1.1455068>.
 - 37 K. Park and D. A. Huse, *Phys. Rev. B* **64**, 134522 (2001), URL <https://link.aps.org/doi/10.1103/PhysRevB.64.134522>.
 - 38 S. E. Korshunov, *Phys. Rev. B* **65**, 054416 (2002), URL <https://link.aps.org/doi/10.1103/PhysRevB.65.054416>.
 - 39 A. Andreanov and M. V. Fistul, *Phys. Rev. B* **102**, 140405 (2020), URL <https://link.aps.org/doi/10.1103/PhysRevB.102.140405>.
 - 40 F.-F. Song and G.-M. Zhang, *Phys. Rev. B* **108**, 014424 (2023), URL <https://link.aps.org/doi/10.1103/PhysRevB.108.014424>.
 - 41 J. Villain, *Journal of Physics C: Solid State Physics* **10**, 1717 (1977), URL <https://doi.org/10.1088/0022-3719/10/10/014>.
 - 42 K. Binder and A. P. Young, *Rev. Mod. Phys.* **58**, 801 (1986), URL <https://link.aps.org/doi/10.1103/RevModPhys.58.801>.
 - 43 A. H. Hartmann and H. Rieger, *Approximation Methods for Spin Glasses* (John Wiley & Sons, Ltd, 2001), chap. 9, pp. 185–226, ISBN 9783527600878, <https://onlinelibrary.wiley.com/doi/pdf/10.1002/3527600876.ch9>, URL <https://onlinelibrary.wiley.com/doi/abs/10.1002/3527600876.ch9>.
 - 44 R. H. Swendsen and J.-S. Wang, *Phys. Rev. Lett.* **58**, 86 (1987), URL <https://link.aps.org/doi/10.1103/PhysRevLett.58.86>.
 - 45 U. Wolff, *Phys. Rev. Lett.* **62**, 361 (1989), URL <https://link.aps.org/doi/10.1103/PhysRevLett.62.361>.
 - 46 G. Rakala and K. Damle, *Phys. Rev. E* **96**, 023304 (2017), URL <https://link.aps.org/doi/10.1103/PhysRevE.96.023304>.
 - 47 L. Vanderstraeten, B. Vanhecke, and F. Verstraete, *Phys. Rev. E* **98**, 042145 (2018), URL <https://link.aps.org/doi/10.1103/PhysRevE.98.042145>.
 - 48 B. Vanhecke, J. Colbois, L. Vanderstraeten, F. Verstraete, and F. Mila, *Phys. Rev. Research* **3**, 013041 (2021), URL <https://link.aps.org/doi/10.1103/PhysRevResearch.3.013041>.
 - 49 J. Colbois, B. Vanhecke, L. Vanderstraeten, A. Smerald, F. Verstraete, and F. Mila, *Phys. Rev. B* **106**, 174403 (2022), URL <https://link.aps.org/doi/10.1103/PhysRevB.106.174403>.
 - 50 H. W. J. Blote and H. J. Hilborst, *Journal of Physics A: Mathematical and General* **15**, L631 (1982), URL <https://dx.doi.org/10.1088/0305-4470/15/11/011>.
 - 51 J. T. Chalker, in *Topological Aspects of Condensed Matter Physics: Lecture Notes of the Les Houches Summer School: Volume 103, August 2014* (Oxford University Press, 2017), ISBN 9780198785781, <https://academic.oup.com/book/0/chapter/203968137/chapter-pdf/45121870/acprof-9780198785781-chapter-3.pdf>, URL <https://doi.org/10.1093/acprof:oso/9780198785781.003.0003>.
 - 52 V. Zauner-Stauber, L. Vanderstraeten, M. T. Fishman, F. Verstraete, and J. Haegeman, *Phys. Rev. B* **97**, 045145 (2018), URL <https://link.aps.org/doi/10.1103/PhysRevB.97.045145>.
 - 53 L. Vanderstraeten, J. Haegeman, and F. Verstraete, *SciPost Phys. Lect. Notes* p. 7 (2019), URL <https://scipost.org/10.21468/SciPostPhysLectNotes.7>.
 - 54 A. Nietner, B. Vanhecke, F. Verstraete, J. Eisert, and L. Vanderstraeten, *Quantum* **4**, 328 (2020), ISSN 2521-327X, URL <https://doi.org/10.22331/q-2020-09-21-328>.
 - 55 J. Haegeman and F. Verstraete, *Annual Review of Condensed Matter Physics* **8**, 355 (2017), <https://doi.org/10.1146/annurev-conmatphys-031016-025507>, URL <https://doi.org/10.1146/annurev-conmatphys-031016-025507>.
 - 56 H. H. Zhao, Z. Y. Xie, Q. N. Chen, Z. C. Wei, J. W. Cai, and T. Xiang, *Phys. Rev. B* **81**, 174411 (2010), URL <https://link.aps.org/doi/10.1103/PhysRevB.81.174411>.
 - 57 M. Levin and C. P. Nave, *Phys. Rev. Lett.* **99**, 120601 (2007), URL <https://link.aps.org/doi/10.1103/PhysRevLett.99.120601>.
 - 58 J. F. Yu, Z. Y. Xie, Y. Meurice, Y. Liu, A. Denblyker, H. Zou, M. P. Qin, J. Chen, and T. Xiang, *Phys. Rev. E* **89**, 013308 (2014), URL <https://link.aps.org/doi/10.1103/PhysRevE.89.013308>.
 - 59 L. Vanderstraeten, B. Vanhecke, A. M. Läuchli, and F. Verstraete, *Phys. Rev. E* **100**, 062136 (2019), URL <https://link.aps.org/doi/10.1103/PhysRevE.100.062136>.
 - 60 M. T. Fishman, L. Vanderstraeten, V. Zauner-Stauber,

- J. Haegeman, and F. Verstraete, *Phys. Rev. B* **98**, 235148 (2018), URL <https://link.aps.org/doi/10.1103/PhysRevB.98.235148>.
- ⁶¹ J. M. Kosterlitz and D. J. Thouless, *Journal of Physics C: Solid State Physics* **6**, 1181 (1973), URL <https://dx.doi.org/10.1088/0022-3719/6/7/010>.
- ⁶² J. M. Kosterlitz, *Journal of Physics C: Solid State Physics* **7**, 1046 (1974), URL <https://dx.doi.org/10.1088/0022-3719/7/6/005>.
- ⁶³ P. Minnhagen, *Reviews of Modern Physics* **59**, 1001 (1987).
- ⁶⁴ A. Vallat and H. Beck, *Physical Review B* **50**, 4015 (1994).
- ⁶⁵ J. Villain, *Journal of Physics C: Solid State Physics* **10**, 4793 (1977), URL <https://doi.org/10.1088/0022-3719/10/23/013>.
- ⁶⁶ T. Obuchi and H. Kawamura, *Journal of the Physical Society of Japan* **81**, 054003 (2012), <https://doi.org/10.1143/JPSJ.81.054003>, URL <https://doi.org/10.1143/JPSJ.81.054003>.
- ⁶⁷ J.-P. Lv, T. M. Garoni, and Y. Deng, *Phys. Rev. B* **87**, 024108 (2013), URL <https://link.aps.org/doi/10.1103/PhysRevB.87.024108>.
- ⁶⁸ I. Maccari, N. Defenu, L. Benfatto, C. Castellani, and T. Enss, *Physical Review B* **102**, 104505 (2020), URL <https://link.aps.org/doi/10.1103/PhysRevB.102.104505>.
- ⁶⁹ I. Maccari, N. Defenu, C. Castellani, and T. Enss, *Journal of Physics: Condensed Matter* **35**, 334001 (2023), URL <https://dx.doi.org/10.1088/1361-648X/acd295>.
- ⁷⁰ P. Minnhagen, *Physical Review B* **32**, 3088 (1985).
- ⁷¹ P. Minnhagen, *Physical Review Letters* **54**, 2351 (1985).
- ⁷² G.-M. Zhang, H. Chen, and X. Wu, *Phys. Rev. B* **48**, 12304 (1993), URL <https://link.aps.org/doi/10.1103/PhysRevB.48.12304>.
- ⁷³ R. H. Swendsen, *Physical Review Letters* **49**, 1302 (1982).
- ⁷⁴ J.-R. Lee and S. Teitel, *Physical Review Letters* **64**, 1483 (1990).
- ⁷⁵ J.-R. Lee and S. Teitel, *Physical Review Letters* **66**, 2100 (1991).
- ⁷⁶ J. Lidmar and M. Wallin, *Physical Review B* **55**, 522 (1997).
- ⁷⁷ G. Kohring, R. E. Shrock, and P. Wills, *Physical Review Letters* **57**, 1358 (1986).
- ⁷⁸ S. R. Shenoy, *Physical Review B* **42**, 8595 (1990).
- ⁷⁹ A. Kamlapure, M. Mondal, M. Chand, A. Mishra, J. Jesudasan, V. Bagwe, L. Benfatto, V. Tripathi, and P. Raychaudhuri, *Applied Physics Letters* **96**, 072509 (2010).
- ⁸⁰ M. Mondal, S. Kumar, M. Chand, A. Kamlapure, G. Saraswat, G. Seibold, L. Benfatto, and P. Raychaudhuri, *Physical Review Letters* **107**, 217003 (2011).
- ⁸¹ M. T. Chen, J. M. Roesler, and J. M. Mochel, *Journal of Low Temperature Physics* **89**, 125 (1992), URL <https://doi.org/10.1007/BF00692584>.
- ⁸² S.-C. Zhang, *Physical Review Letters* **71**, 2142 (1993), URL <https://link.aps.org/doi/10.1103/PhysRevLett.71.2142>.
- ⁸³ M. Gabay and A. Kapitulnik, *Physical Review Letters* **71**, 2138 (1993), URL <https://link.aps.org/doi/10.1103/PhysRevLett.71.2138>.
- ⁸⁴ S. S. Botelho and C. A. R. Sá de Melo, *Physical Review Letters* **96**, 040404 (2006).
- ⁸⁵ R. Hivet, E. Cancellieri, T. Boulier, D. Ballarini, D. Sanvitto, F. M. Marchetti, M. H. Szymanska, C. Ciuti, E. Giacobino, and A. Bramati, *Phys. Rev. B* **89**, 134501 (2014), URL <https://link.aps.org/doi/10.1103/PhysRevB.89.134501>.
- ⁸⁶ E. Granato and J. M. Kosterlitz, *Physical Review B* **33**, 4767 (1986).
- ⁸⁷ E. Granato, *Journal of Physics C: Solid State Physics* **20**, L215 (1987).
- ⁸⁸ J. Lee, E. Granato, and J. M. Kosterlitz, *Physical Review B* **44**, 4819 (1991).
- ⁸⁹ M. S. Li and M. Cieplak, *Physical Review B* **50**, 955 (1994).
- ⁹⁰ M. P. Nightingale, E. Granato, and J. M. Kosterlitz, *Physical Review B* **52**, 7402 (1995).
- ⁹¹ B. I. Halperin and D. R. Nelson, *Phys. Rev. Lett.* **41**, 121 (1978), URL <https://link.aps.org/doi/10.1103/PhysRevLett.41.121>.
- ⁹² D. R. Nelson and B. I. Halperin, *Phys. Rev. B* **19**, 2457 (1979), URL <https://link.aps.org/doi/10.1103/PhysRevB.19.2457>.
- ⁹³ A. P. Young, *Phys. Rev. B* **19**, 1855 (1979), URL <https://link.aps.org/doi/10.1103/PhysRevB.19.1855>.
- ⁹⁴ T. Mizoguchi, L. D. C. Jaubert, and M. Udagawa, *Phys. Rev. Lett.* **119**, 077207 (2017), URL <https://link.aps.org/doi/10.1103/PhysRevLett.119.077207>.
- ⁹⁵ K. Tokushuku, T. Mizoguchi, and M. Udagawa, *Phys. Rev. B* **100**, 134415 (2019), URL <https://link.aps.org/doi/10.1103/PhysRevB.100.134415>.
- ⁹⁶ K. Tokushuku, T. Mizoguchi, and M. Udagawa, *Journal of the Physical Society of Japan* **89**, 053708 (2020), <https://doi.org/10.7566/JPSJ.89.053708>, URL <https://doi.org/10.7566/JPSJ.89.053708>.
- ⁹⁷ J. T. Chalker, P. C. W. Holdsworth, and E. F. Shender, *Phys. Rev. Lett.* **68**, 855 (1992), URL <https://link.aps.org/doi/10.1103/PhysRevLett.68.855>.
- ⁹⁸ J. Pitts, F. L. Buessen, R. Moessner, S. Trebst, and K. Shtengel, *Phys. Rev. Res.* **4**, 043019 (2022), URL <https://link.aps.org/doi/10.1103/PhysRevResearch.4.043019>.